AGU PUBLICATIONS

JGR

Journal of Geophysical Research: Solid Earth

RESEARCH ARTICLE
10.1002/2015JB011941

Key Points:
- Pre-Landers triangulation/EDM data used to constrain Mojave secular deformation
- Excessive right shear found in Landers/HM rupture in GPS postseismic velocities
- Results provide new constraints on Mojave lithosphere rheological structure

Supporting Information:
- Text S1–S7, Tables S1–S28, and Figures S1–S49

Correspondence to:
Z.-K. Shen,
zshen@ucla.edu

Citation:
Liu, S., Z.-K. Shen, and R. Bürgmann (2015), Recovery of secular deformation field of Mojave Shear Zone in Southern California from historical terrestrial and GPS measurements, *J. Geophys. Res. Solid Earth*, *120*, 3965–3990, doi:10.1002/2015JB011941.

Received 7 FEB 2015
Accepted 14 APR 2015
Accepted article online 22 APR 2015
Published online 28 MAY 2015

Recovery of secular deformation field of Mojave Shear Zone in Southern California from historical terrestrial and GPS measurements

Shaozhuo Liu[1], Zheng-Kang Shen[2,3], and Roland Bürgmann[4]

[1]State Key Laboratory of Earthquake Dynamics, Institute of Geology, China Earthquake Administration, Beijing, China, [2]Department of Earth, Planetary, and Space Sciences, University of California, Los Angeles, California, USA, [3]School of Earth and Space Science, Peking University, Beijing, China, [4]Department of Earth and Planetary Science, University of California, Berkeley, California, USA

Abstract The 1992 M_w 7.3 Landers and 1999 M_w 7.1 Hector Mine earthquakes struck the Eastern California Shear Zone (ECSZ) in the Mojave Desert, Southern California. Coseismic and postseismic deformation from these events affect efforts to use Global Positioning System (GPS) observations collected since these events to establish a secular surface velocity field, especially in the near field of the coseismic ruptures. We devise block motion models constrained by both historical pre-Landers triangulation and trilateration observations and post-Landers GPS measurements to recover the secular deformation field and differentiate the postseismic transients in the Mojave region. Postseismic transients are found to remain in the Southern California Earthquake Center Crustal Motion Map Version 4, Plate Boundary Observatory, and Scripps Orbit and Permanent Array Center GPS velocity solutions in the form of 2–3 mm/yr excess right-lateral shear across the Landers and Hector Mine coseismic ruptures. The cumulative deformation rate across the Mojave ECSZ is 13.2–14.4 mm/yr, at least twice the geologic rate since the late Pleistocene ($\leq 6.2 \pm 1.9$ mm/yr). Postseismic GPS time series based on our secular velocity field reveal enduring late-stage transient motions in the near field of the coseismic ruptures that provide new constraints on the rheological structure of the lower crust and upper mantle.

1. Introduction

Geologic and geodetic studies reveal the active deformation of the Mojave section of the Eastern California Shear Zone (Mojave ECSZ) in the Mojave Desert, Southern California [*Sauber et al.*, 1986; *Dokka and Travis*, 1990a; *Savage et al.*, 1990] (Figure 1). The Mojave ECSZ consists of several subparallel Cenozoic strike-slip faults, which have accommodated 6–12 mm/yr of dextral slip since the late Miocene [*Dokka and Travis*, 1990a, 1990b] and $\leq 6.2 \pm 1.9$ mm/yr since the late Pleistocene [*Oskin et al.*, 2008]. The Mojave ECSZ plays a secondary role in accommodating the Pacific-North America relative plate motion of ~47 mm/yr at ~34°N–35.5°N latitude [*DeMets et al.*, 1994], which is predominately accommodated by the nearby San Andreas fault (SAF) system. Compared with more localized deformation across most sections of the SAF in California, deformation in the Mojave ECSZ is broadly distributed [*Sauber et al.*, 1994; *Shen et al.*, 2011].

The Mojave ECSZ was struck by the 1992 M_w 7.3 Landers [*Sieh et al.*, 1993] and 1999 M_w 7.1 Hector Mine earthquakes [*Scientists from the U.S. Geological Survey et al.*, 2000]. Prior to this earthquake sequence, the Mojave ECSZ was seismically quiet during 1769–1992, with only a few recorded moderate-sized earthquakes in the Mojave Desert: the 1947 Manix M_L 6.2 earthquake east of Barstow [*Ellsworth*, 1990] and the Homestead Valley sequence in 1983 ($M_L = 4.9$, 5.2, 4.5, 4.8) [*Stein and Lisowski*, 1983]. In the bordering areas of the Mojave Desert, the Mojave section of the SAF ruptured in the 1812 M_w 7.3 Wrightwood and 1857 M_w 7.9 Great Fort Tejon earthquakes and the White Wolf fault ruptured in the 1952 M_w 7.3 Kern Country earthquake [*Toppozada et al.*, 2002]. The 1872 M_w 7.4–7.9 Owens Valley earthquake ruptured a ~120 km long section of the northward continuation of the ECSZ north of 36°N [*Hough and Hutton*, 2008].

The distribution of interseismic deformation across the Mojave ECSZ is constrained by geodetic observations (Figure 1). Prior to the 1992 Landers earthquake, the deformation field was mainly determined using triangulation and trilateration methods [*Sauber et al.*, 1986; *Savage et al.*, 1990; *Sauber et al.*, 1994]. The measurements from the 1930s to the 1980s suggest cumulative slip rates of ~6.7–12 mm/yr across the

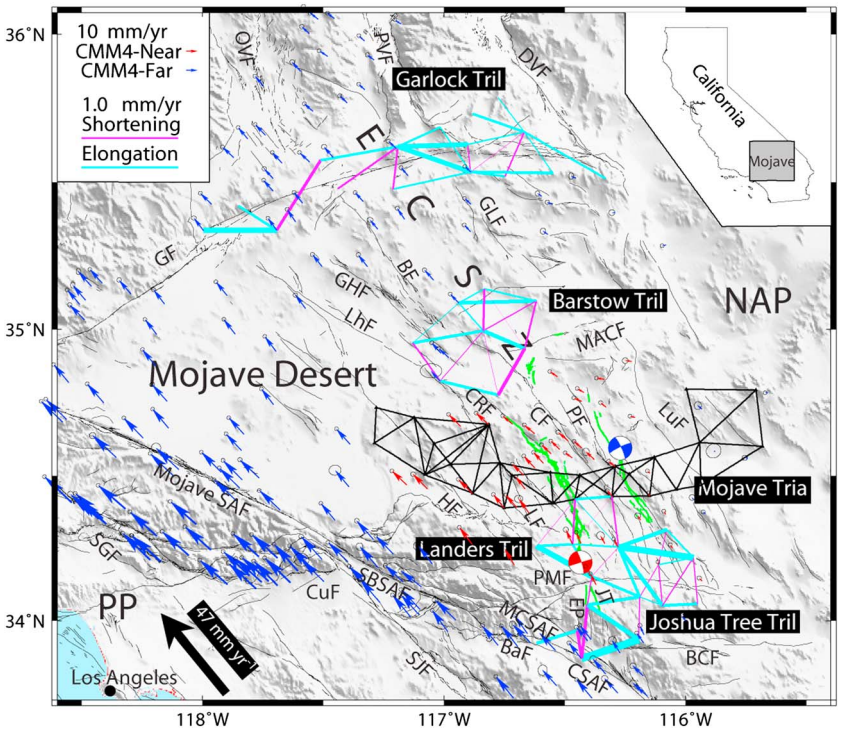

Figure 1. Tectonic setting of the Mojave Desert, Southern California. The thin black lines are Quaternary active faults [*Jennings and Saucedo*, 1994], and the green lines are the coseismic ruptures of the 1992 Landers and 1999 Hector Mine earthquakes. The red and blue beach balls indicate the focal mechanisms of the Landers and Hector Mine earthquakes, respectively. The Eastern California Shear Zone (ECSZ) is a transitional deformation zone sandwiched between the Pacific Plate (PP) and the North American plate (NAP). The black vector shows the NUVEL-1A PP-NAP relative plate motion [*DeMets et al.*, 1994]. Faults in the vicinity of the Mojave Desert are the following: HF = Helendale, LF = Lenwood, CRF = Camp Rock, CF = Calico, PF = Pisgah, LuF = Ludlow, BF = Blackwater, GHF = Gravel Hills, LhF = Lockhart, GLF = Goldstone Lake, MACF = Manix-Afton Canyon, CSAF = Coachella SAF, Mojave SAF = Mojave SAF, SBSAF = San Bernardino SAF, MCSAF = Mission Creek SAF, BaF = Banning, SJF = San Jacinto, EP = Eureka Peak, JT = Joshua Tree, PMF = Pinto Mountain, BCF = Blue Cut, GF = Garlock, OVF = Owens Valley, PVF = Panamint Valley, DVF = Death Valley, CuF = Cucamonga, SGF = San Gabriel. The Mojave triangulation network (Mojave Tria) is shown by the black polygons in the central Mojave. The cyan and magenta lines represent elongation and shortening of trilateration baselines (Barstow Tril, Landers Tril, Joshua Tree Tril, and Garlock Tril), respectively, with line width proportional to the magnitude of elongation and shortening. The near-field and far-field GPS velocities relative to the Stable North American Reference Frame (CMM4 [*Shen et al.*, 2011]), with error ellipses at 95% confidence, are also shown by the red and blue vectors.

Mojave ECSZ. The wide range of derived slip rates arises from the limited spatial coverage of the geodetic networks, the different methods used, and assumptions made about the spatial distribution of the shear zone. Multiplying the measured shear strain rate and the width of the assumed shear zone yielded 6.7 ± 1.3 mm/yr across a shear zone of ~40 km [*Sauber et al.*, 1986] and ~8.0 mm/yr across a 60 km wide shear zone [*Savage et al.*, 1990], respectively. A follow-up 2-D model analysis of the strain rate data proposes buried distributed shear of ~12 mm/yr below a locking depth of 10–15 km across a ~60.0 km wide shear zone [*Sauber et al.*, 1994].

GPS observations have been made in Southern California since 1986 and proliferated in the last two decades due to the increased continuous GPS (cGPS) observations made by the Southern California Integrated GPS Network (SCIGN, http://www.scec.org/scign/) and the Plate Boundary Observatory (PBO) GPS network (http://www.earthscope.org/science/observatories/pbo). The geodesy group of Southern California Earthquake Center (SCEC) processed all the available GPS data and released a series of products documenting estimates of the secular, interseismic velocity field together with coseismic and postseismic displacements from major earthquakes that occurred during the observation periods [*Shen et al.*, 1997]. The latest result was the solution of the SCEC Crustal Motion Map Version 4 (CMM4) incorporating all the campaign GPS data 1986–2004 [*Shen et al.*, 2011]. These GPS velocity data offered up to 1–2 mm/yr

accuracy for description of the secular deformation field in Southern California except in the Mojave ECSZ region. The estimates of secular velocities in the Mojave ECSZ are more uncertain and/or biased, because the SCEC Crustal Motion Maps are mainly derived from post-Landers GPS observations, which in the Mojave ECSZ are influenced by the postseismic transients of the Landers and Hector Mine earthquakes [*Shen et al*., 2011]. The Scripps Orbit and Permanent Array Center (SOPAC) and the PBO Analysis Center Coordinator at Massachusetts Institute of Technology independently released interseismic velocity solutions of the SCIGN and PBO cGPS sites and position time series until recent years (http://sopac.ucsd.edu/dataArchive/andpbo.final_snf01.vel, ftp://data-out.unavco.org/pub/products/velocity/). Therefore, the SOPAC and PBO products provide additional constraints on the regional deformation field in the last decade since 2004, when the CMM4 GPS time series end.

A series of kinematic deformation models of Southern California has been developed constrained by GPS velocity data. These models can be classified into two groups: block motion and non–block motion models. Standard block motion models estimate angular block-rotation parameters while considering the elastic strain buildup from shallowly locked block-bounding faults [*McClusky et al*., 2001; *Miller et al*., 2001; *Becker et al*., 2005; *Meade and Hager*, 2005; *Spinler et al*., 2010; *Loveless and Meade*, 2011; *Johnson*, 2013]. Some block models allow for either uniform [e.g., *McCaffrey*, 2005] or distributed [*Chuang and Johnson*, 2011; *Johnson*, 2013] strain rates across each block in addition to the block rotation and elastic strain that are prescribed in the standard block models. Other studies of nonblock motion models utilize kinematic finite element modeling [*Bird*, 2009] and linked and buried dislocations beneath faults' locking depth [*Zeng and Shen*, 2014]. Most of the geodetic deformation models yield geodetic slip rates of 12–18 mm/yr summed across the Mojave ECSZ, which are significantly higher than the late Pleistocene slip rates of ~6 mm/yr. Such a large contrast was considered a geologic-geodetic slip rate discrepancy [*Meade and Hager*, 2005; *Dolan et al*., 2007; *Oskin et al*., 2008], which gave rise to extensive debates regarding the short- and long-term deformation in the Mojave ECSZ.

Resolving the geologic-geodetic discrepancy requires thorough investigation of geologic, geodetic, and geophysical constraints. The discrepancy could be due to time-dependent earthquake-cycle deformation. The interseismic deformation measured by GPS observations within the Mojave Desert represents a snapshot of deformation early in an earthquake cycle [*Chuang and Johnson*, 2011; *Johnson*, 2013], containing postseismic transients of recurring large earthquakes in the region [*Hearn et al*., 2013]. On the other hand, part of the discrepancy could be due to distributed off-fault deformation [*Bird*, 2009; *Herbert et al*., 2013; *Johnson*, 2013; *Herbert et al*., 2014].

An accurate description of the secular deformation field is crucial for understanding the tectonics and associated seismic hazard in the Mojave area. The CMM velocity fields removed short-period post-Landers and post-Hector Mine deformation; but as described in the subsequent Data section (section 2.2, GPS Data), they may still contain residual signals of postseismic deformation from the recent events. Previous geodetic models using these CMM velocity products did not assess to what degree the postseismic transients of the Landers and Hector Mine earthquakes might have contaminated their model estimates of the Mojave ECSZ fault slip rates. Without accurate data sets, it is difficult to distinguish possible origins of the geologic-geodetic slip rate discrepancy as invoked in previous studies.

One goal of this effort to derive an accurate description of the secular deformation field is to also obtain a more accurate characterization of the postseismic deformation, which is essential for the understanding of the physical processes associated with postseismic relaxation. Models of postseismic geodetic observations with sufficient spatiotemporal coverage and resolution provide constraints on the rheology of the lower crust and upper mantle [e.g., *Bürgmann and Dresen*, 2008]. This requires an accurate description of the interseismic deformation just prior to the recent earthquakes. The temporal evolution of postseismic deformation is quite uncertain in the near field of the Landers and Hector Mine earthquakes as the secular deformation field was not measured directly [*Savage and Svarc*, 2009]. Discernable postseismic deformation extends to the Yucca Mountain area in Nevada, ~200 km from the epicenter [*Freed et al*., 2007; *Hammond et al*., 2010]. Postseismic deformation mechanisms invoked for the Landers earthquake include (1) fault afterslip [*Shen et al*., 1994; *Savage and Svarc*, 1997], (2) fault zone collapse [*Massonnet et al*., 1996], (3) poroelastic rebound and afterslip [*Peltzer et al*., 1998; *Fialko*, 2004], (4) viscoelastic relaxation in the lower crust [*Deng et al*., 1998], and predominantly in the upper mantle

[*Pollitz et al*., 2000]. For the 1999 Hector Mine earthquake, three types of processes have been considered, including (1) viscoelastic relaxation predominantly in the upper mantle [e.g., *Pollitz et al*., 2001; *Pollitz*, 2003; *Freed and Burgmann*, 2004; *Freed et al*., 2007], (2) afterslip on the deep [*Owen et al*., 2002; *Perfettini and Avouac*, 2007] and shallow parts of the fault [*Jacobs et al*., 2002], and (3) poroelastic rebound and viscoelastic relaxation in the lower crust [*Masterlark and Wang*, 2002].

The questions raised above encourage us to test for postseismic transients left in the CMM4 and other GPS velocity fields and to derive an accurate secular velocity field (interseismic velocities just prior to the recent earthquakes) in the Mojave Desert, especially in the near field of the Landers and Hector Mine ruptures. Model predictions of elastic block motion models constrained by both historical pre-Landers triangulation/trilateration observations across the Mojave ECSZ and postseismic GPS data outside of the Landers/Hector Mine fault zone are used to establish this secular velocity field, which is aided by cluster analysis of the GPS velocities.

2. Data

2.1. Pre-Landers Historical Geodetic Data

2.1.1. Triangulation Strain Rate Data

We use shear-strain rate data from the central Mojave triangulation network to improve the spatial coverage of pre-Landers observations in the Landers and Hector Mine epicentral areas [*Sauber et al*., 1986, 1994] (Figures 1 and 3 and Table S1 in the supporting information). This network spans several subparallel faults in the central Mojave, extending from a few kilometers west of the Helendale fault to the east of the Ludlow fault. The network was surveyed by the National Geodetic Survey between 1934 and 1940 and again in 1965; the U.S. Geological Survey conducted a trilateration survey of the same network in 1982. A unified analysis of both the angle and line-length data [*Sauber et al*., 1994] indicates a roughly constant maximum shear-strain rates (~0.15 μstrain/yr) from the Helendale fault to the Pisgah fault and a much reduced and less certain shear-strain rate of ~0.06 ± 0.06 μstrain/yr within the Pisgah/Ludlow network to the east of the Pisgah fault (Figure 3 and Table S1 in the supporting information). We express the shear strain rates in terms of the engineering strain, which is twice the tensor shear strain.

2.1.2. Trilateration Rates of Line-Length Change Data

We use rates of line-length change derived from trilateration observations made in the Landers [*Savage et al*., 1993], Joshua Tree [*Savage et al*., 1993], Barstow [*King*, 1985; *Savage et al*., 2001], and Garlock networks [*Savage et al*., 2001]. These data provide constraints on deformation within the southern and central Mojave ECSZ, as well as in the northern end spanning the Garlock fault (Figure 1).

The Landers trilateration network, located immediately south of the Landers subnetwork of the Mojave triangulation network, was observed using electro-optical distance measurement (EDM) instruments in 1979, 1980, 1981, 1988, and 1992, just prior to and 3 months after the Landers earthquake [*Savage et al*., 1993]. To the south and east of the Landers trilateration network, the Joshua Tree network had been surveyed several times since 1973 until 3 months after the Landers earthquakes [*Savage et al*., 1993]. To the north of the Mojave triangulation network and within the Mojave ECSZ is the Barstow trilateration network, which was surveyed by the U.S. Geological Survey from 1979 to 1989 [*Savage et al*., 2001]. Repeated observations were made in the Garlock trilateration network spanning the central and eastern Garlock fault from 1973 to 1990 [*Savage et al*., 2001]. For the Landers and Joshua Tree networks, we exclude large blunders and then correct coseismic offsets in the original mark-to-mark distance time series using dislocation models of the 1979 Homestead Valley, 1986 North Palm Springs, and 1992 Joshua Tree earthquakes [*Savage et al*., 1993]. All the observations in the Barstow and Garlock networks are retained. See Text S1 in the supporting information for a detailed description of the determination of rates of line-length change.

The random errors in the mark-to-mark distance observations are assumed to follow a normal distribution with zero mean and variance given by

$$\sigma^2 = a^2 + b^2 L^2 \tag{1}$$

where L is the baseline distance (in millimeters) and a and b are constants ($a = 3$ mm and $b = 2 \times 10^{-7}$ [*Savage et al*., 1993]). The variances of all the observations are shown as error bars in figures of the line-length time series (Figures S2–S5 and Text S1 in the supporting information).

A least squares fit is used to estimate the rates of the line-length time series. We assume steady interseismic surface deformation during the observation period and that the line-length change of a specified baseline follows a simple linear function of the form

$$L_i = L_o + k \times t_i \quad (2)$$

where L_i is the mark-to-mark distance made at the time t_i, L_o is a nominal line-length, and k, the rate of line-length change, is estimated. The rates of line-length change derived are shown in Figure 1 and Tables S3–S5 in the supporting information (Text S1 in the supporting information), respectively, for the Landers and Joshua Tree, Barstow, and Garlock networks. Estimated 1-sigma uncertainties of rates smaller than 0.2 mm/yr are raised to 0.2 mm/yr. The fits to the original mark-to-mark distance time series are shown in Figures S3–S5 in the supporting information (Text S1 in the supporting information).

2.2. GPS Data

2.2.1. Postseismic Transients in GPS Velocity-Field Estimates

The 1992 M_w 7.3 Landers and 1999 M_w 7.1 Hector Mine earthquakes significantly altered the deformation field in the Mojave Desert region. The presence of postseismic transients makes it difficult to separate the correlated postseismic signals from secular motions using GPS time series, as shown in a case study at the Yucca Mountain network in southern Nevada [*Hammond et al*., 2010]. The estimates of secular velocities in the Mojave ECSZ are therefore potentially biased using GPS observations made mostly after the 1992 Landers earthquake.

The geodesy group of the Southern California Earthquake Center (SCEC) made adjustments in the two most recent versions of the Crustal Motion Map (CMM3 and CMM4) to account for the postseismic deformation effects of the two earthquakes [*Shen et al*., 2003; *Shen et al*., 2011]. The CMM3 velocities for the Mojave sites were derived omitting 1.5 years of data after the Landers and Hector Mine earthquakes, respectively, to prevent the velocity estimates from being contaminated by the immediate postseismic deformation. However, the velocity estimates may still be affected to a certain degree by longer-term postseismic deformation effects [*Shen et al*., 2003]. The CMM4 velocities were obtained from the station position time series that are characterized by a functional which includes a secular velocity term and a logarithmic term to represent the postseismic deformation [*Shen et al*., 2011]. If this assumption deviates from reality (i.e., the postseismic signals are not exactly logarithmic), the velocity estimate will be off because of its correlation with the residual long-term postseismic deformation.

To examine the extent to which postseismic transients of the Landers and Hector Mine earthquakes affect the CMM4 GPS velocity field, we first use a modified method of *Shen et al*. [1996] that allows for spatially variable smoothing to interpolate the velocity field and obtain a distributed strain rate map in the Mojave Desert and its vicinity [*Shen et al*., 2007] (Figure 2 and Figures S7–S9 in the supporting information). The CMM4 shear-strain rate field clearly shows a concentration in the near field of the Landers and Hector Mine earthquakes. We next assess whether the pre-Landers deformation rates within the triangulation and trilateration networks are compatible with the corresponding values derived from the CMM4 GPS velocity field. We use the method of *Shen et al*. [2007] to interpolate the CMM4 GPS velocity field and derive the velocities at sites of the triangulation/trilateration networks (see Text S2 in the supporting information for CMM4 GPS-derived pre-Landers deformation field). Assuming a uniform strain rate within each triangulation subnetwork (Figure 3), the predicted triangulation site velocities are used to estimate the maximum shear-strain rate in the network using least squares (Text S2 in the supporting information). The result shows that in the immediate near field of the Landers rupture, the CMM4-derived maximum shear-strain rates are significantly higher than the observed pre-Landers values. In the Camp Rock and Landers triangulation networks (numbered 2 and 3 in Figure 3), the derived CMM4 shear strain rates are 0.45 ± 0.02 μstrain/yr and 0.41 ± 0.02 μstrain/yr, comparing to the pre-Landers rates of 0.16 ± 0.06 μstrain/yr and 0.22 ± 0.09 μstrain/yr, respectively. It is noteworthy that the high level of shear strain rate derived from CMM4 GPS velocities is not discerned in the Calico/Pisgah triangulation network that is an ~15 km aperture network across the coseismic rupture of the Hector Mine earthquake (network number 4 in Figure 3).

The CMM4-predicted trilateration site velocities are reduced to the rates of line-length change of baselines within the Landers, Joshua Tree, Barstow, and Garlock trilateration networks (Text S2 in the supporting

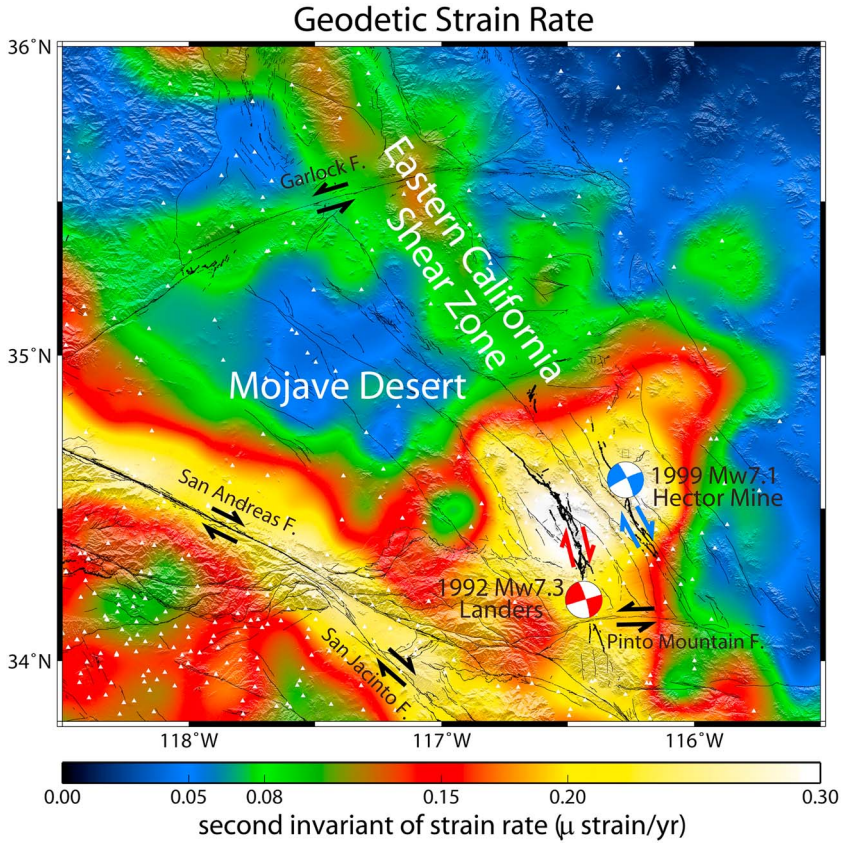

Figure 2. Mapview of the second invariant of strain rates estimated from CMM4 GPS velocity field. The red and blue beach balls indicate the focal mechanisms of the Landers and Hector Mine earthquakes, respectively. The white triangles show the locations of GPS stations used for velocity interpolation.

information). The CMM4 predicted rates indicate prominent right-lateral shear motion across a northwest trending plane, which differs from modest right-lateral shear indicated by the pre-Landers data in the Landers trilateration network (Figure S3 and Table S3 in the supporting information). Most of the CMM4-derived line-length change rates are consistent with the pre-Landers rates in the Joshua Tree, Barstow, and Garlock trilateration networks (Figures S3–S5 and Tables S3–S5 in the supporting information).

For a better visual comparison of the pre-earthquake and post-earthquake data sets, we transform the pre-Landers rates of line-length change into relative velocities using a model coordinate solution [*Segall and Matthews*, 1988] with the interpolated CMM4 velocities to constrain the null-space (Figure 4). This comparison clearly shows again that the CMM4 GPS velocities in the near field of the Landers earthquake and near the southern end of the Hector Mine earthquake contain significant postseismic transients. CMM4 GPS velocities in the other regions of the Mojave Desert away from the Landers/Hector Mine fault zone contain less discernable postseismic transients.

In section 5.2 (comparison with other velocity fields), we will test the extent to which the postseismic transients still linger in the other four GPS velocity solutions derived mostly from GPS observations since 2005.

2.2.2. Cluster Analysis of the Mojave CMM4 GPS Velocities

The statistical cluster analysis has been applied to find GPS velocity clusters that may coincide with and help define fault-bounded blocks [*Simpson et al.*, 2012; *Savage and Simpson*, 2013a, 2013b]. We use the *k*-medoids method to find clusters in the CMM4 GPS velocities and define the block models (Text S3 in the supporting information). The major differences between the CMM4 GPS velocities (Figure S10 in the supporting information) and the U.S. Geological Survey (USGS) GPS data set used in a previous cluster analysis in the Mojave region [*Savage and Simpson*, 2013b] are that (1) they span different postseismic periods (CMM4: 1992–2004 versus USGS data set: 2000–2012); (2) the CMM4 data set was generated with attempts to model and remove the postseismic effects, whereas no adjustment was applied to the

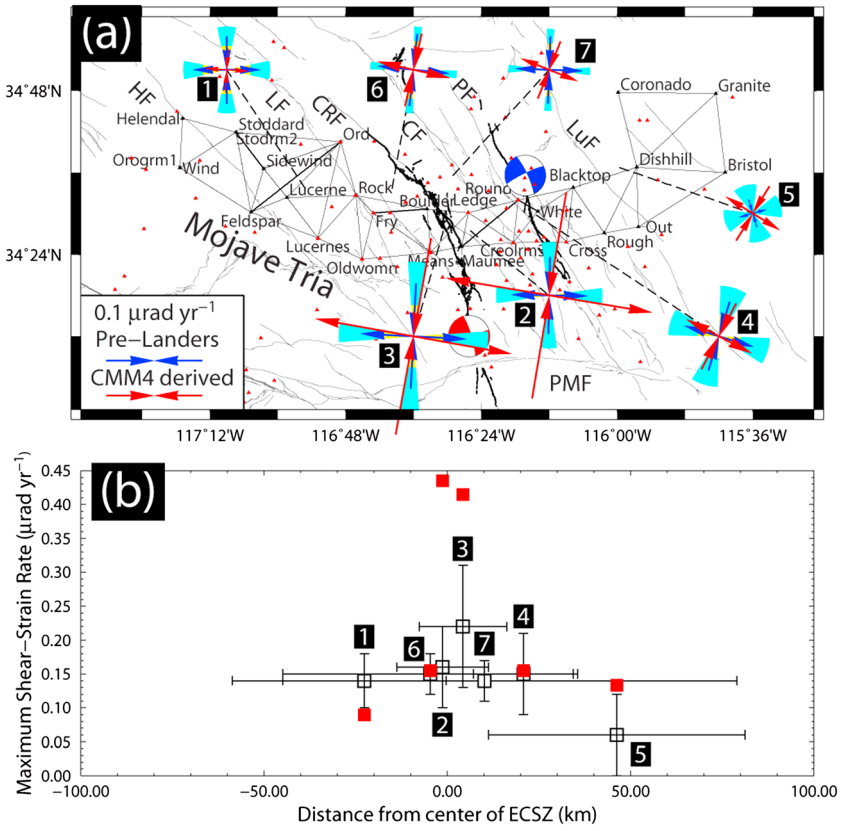

Figure 3. Comparison of maximum shear-strain rates within the Mojave triangulation network. (a) Pre-Landers (blue cross vectors) and predicted (red cross vectors) maximum shear-strain rates derived from historical geodetic observations and from the interpolated CMM4 GPS velocity field, respectively. The fan-shaped sectors in cyan sector indicate the one-sigma uncertainties of the principal strain rates. The numbers denote the subnetworks labeled in the first column of Table S1. The red triangles show the locations of GPS stations used for velocity interpolation. The red and blue beach balls indicate the focal mechanisms of the Landers and Hector Mine earthquakes, respectively. The thick black lines represent the coseismic ruptures of the Landers and Hector Mine earthquakes, respectively. (b) Maximum shear-strain rate profile across the Mojave ECSZ. The *x* axis is the distance along profile which is perpendicular to the strike of the shear zone. The open squares and the vertical error bars are the pre-Landers maximum shear-strain rates and their one-sigma uncertainties, and the horizontal bars show the geographic spans of the subnetworks. The red squares indicate the predicted maximum shear-strain rates as mentioned in Figure 3a.

USGS data set; (3) the CMM4 data set provides denser coverage in the near field of the Landers and Hector Mine earthquakes, whereas more stations are located in the Northeast Mojave Domain (NEMD) in the USGS data set.

Text S3 in the supporting information provides the details of the cluster analysis. Figures S12 and S13 show the $k = 2, 3, 4$, and 5 clusters in velocity space and their map locations, respectively. Except for the Goldstone Lake fault and the Hector Mine earthquake rupture, the divisions of clusters do not coincide well with the regional faults (Figure 5 and Figure S13 in the supporting information). The failure of the clustering to find block boundaries consistent with faults in the region may be attributed to closely spaced faults, fault locking effects, and the presence of postseismic transients in the near field of the Landers and Hector Mine earthquakes. When the number of clusters increases ($k \geq 4$), the inferred station clusters mingle with each other in the near field of the Landers and Hector Mine earthquakes, which indicates complexities in the near-field GPS velocities (Figure S13 in the supporting information).

The clustering results roughly agree with the previous cluster analysis of *Savage and Simpson* [2013b]. The differences mostly arise from the different data sets used. The most striking difference is that the $k = 4$ and 5 clustering of the CMM4 GPS velocities do not discern the NEMD. This could be attributed

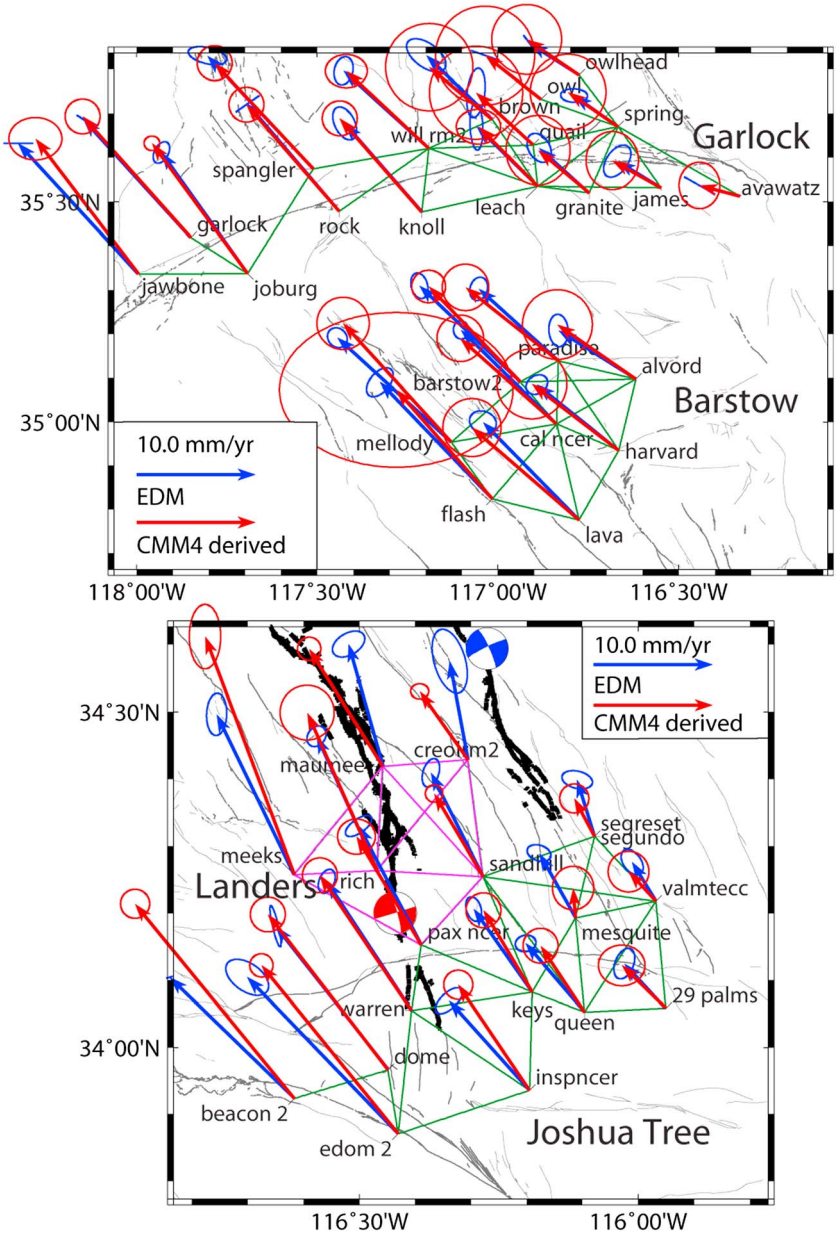

Figure 4. Comparison of station velocities at trilateration sites. The blue vectors are model coordinate solutions with the null parameter space constrained by the CMM4 interpolated station velocities (red vectors). The error ellipses of the velocities are at the 95% confidence. The red and blue beach balls indicate the focal mechanisms of the Landers and Hector Mine earthquakes, respectively. The green lines show the baselines of the Joshua Tree, Barstow, and Garlock trilateration networks. The magenta lines show the baselines of the Landers trilateration network. The thick black lines represent the coseismic ruptures of the Landers and Hector Mine earthquakes, respectively.

to differences in data set used and block geometries adopted in the models. See Text S3 in the supporting information for details.

2.3. Data Compilation

Both GPS and triangulation/trilateration data sets are used in our study and are complementary to each other. The triangulation/trilateration data provide critical constraints across most of the active parts of the Mojave ECSZ but still leave large parts of the regions inside and outside of the shear zone uncovered. The terrestrial data sets, due to their intrinsic limitations, also cannot constrain the overall rotation, translation, and/or dilation of the deformation field. The GPS data set, on the other hand, has a much better spatial coverage

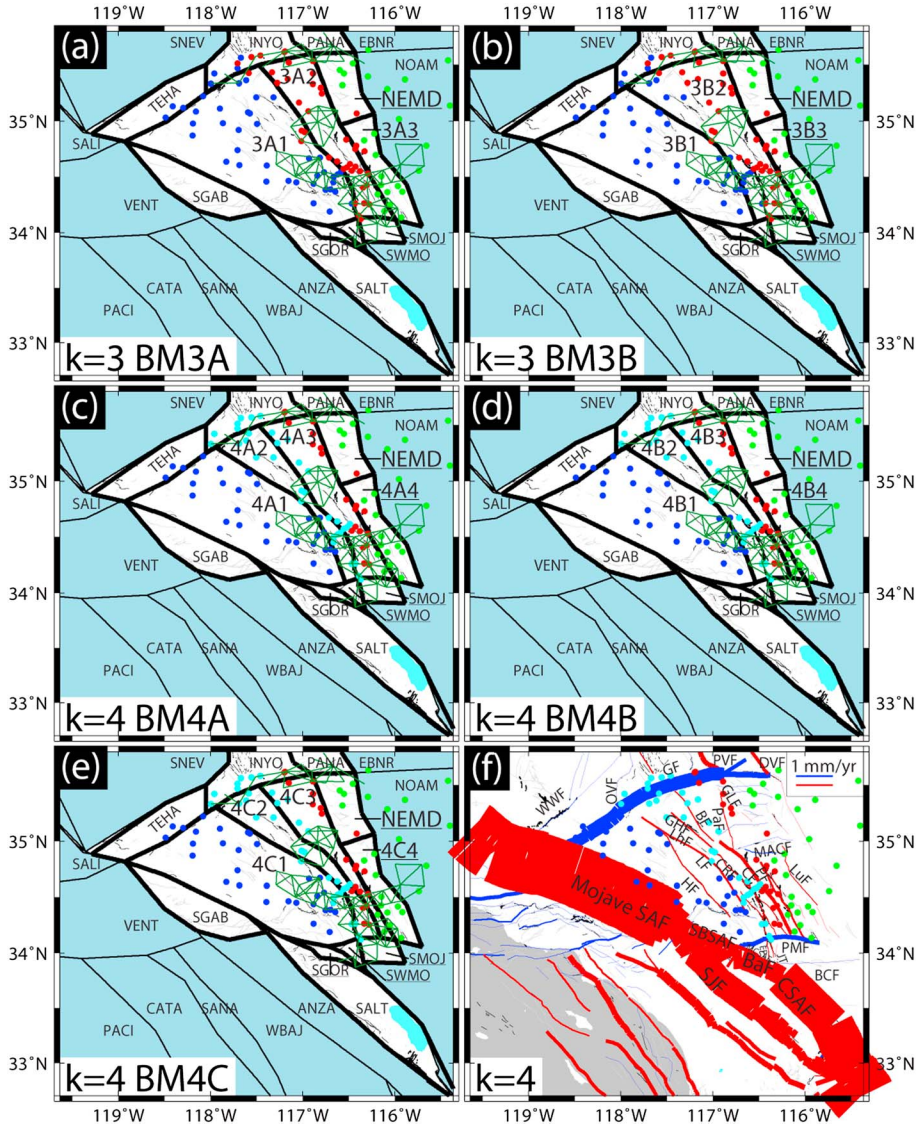

Figure 5. Block model geometries based on the *k*-medoids clustering. Superimposed on subplots are cluster grouping of (a and b) GPS stations of $k = 3$ and 4, respectively, and (c–f) the historic geodetic networks (green lines). The thick black lines show fault segments delineating the block boundaries; abbreviations of block names are also labeled. The blocks outside the greater Mojave region are shadowed by light blue. The UCERF3 fault slip rates (http://pubs.usgs.gov/of/2013/1165/) are shown by colored lines in Figure 5f (the red and blue lines denote the right-lateral slip and left-lateral slip, respectively, and the line widths are proportional to the magnitudes of slip rates). Fault name abbreviations are the same as in Figure 1. WWF: the White Wolf fault.

in the region; is capable of constraining the regional rotation, translation, and dilation; and has better accuracy than the triangulation/trilateration data. The only inferiority of the data set is the potential contamination by the recent postseismic deformation transients. We therefore seek to use the triangulation/trilateration data to improve the constraints on the secular deformation field across the Mojave ECSZ and use the GPS data, previously corrected for postseismic transients with a logarithmic function fit, to constrain deformation in the surrounding region and to stabilize the solution.

We differentiate "near-field" and "far-field" CMM4 GPS stations inside and outside of the Landers/Hector Mine epicentral region. There are 44 near-field and 215 far-field sites as shown by the red and blue arrows, respectively, in Figure 1. The near-field GPS sites are located in the high strain rate region identified in the strain rate calculation using the CMM4 GPS velocities, likely containing appreciable remaining postseismic transients of recent earthquakes as described in section 2.2.1 (Figure 2 and Figures S8 and S9 in the supporting information). They are therefore excluded from the data set used in the model inversions.

In the CMM4 GPS velocity solution, there are a number of cGPS sites whose formal velocity uncertainties are quite small, as low as 0.2 mm/yr or less. Although the statistical analysis of the CMM4 solution was done through a rigorous procedure, other "external errors" such as those due to local geophysical and hydrological perturbations are not accounted for during the process; thus, the uncertainty estimates may be too small to represent the actual GPS data uncertainties in depicting the deformation field. In the following analysis, we therefore scale up the east and north velocity uncertainties of the CMM4 GPS sites to 0.7 mm/yr if they are smaller than that to compensate for such effects.

3. Block Modeling

3.1. Block Motion Models

Crafting block motion models requires specification of the fault-block geometries. Our focus region is the wedge-shaped Mojave Block bounded by the Mojave segment of the San Andreas fault (Mojave SAF), San Bernardino Mountain segment of the San Andreas fault (SBSAF), Pinto Mountain fault (PMF), Ludlow fault (LuF), and Garlock fault (GF) (Figure 5). The elastic strain accumulation of faults in the neighboring areas, however, still contributes to deformation inside the Mojave region. We therefore extend the region of interest to the immediate neighborhood areas of the Mojave Block (hereafter referred to as the greater Mojave region), also considering contributions from the Coachella SAF, San Jacinto, Cucamonga, San Gabriel, White Wolf, Owens Valley, Death Valley, Ludlow, and Blue Cut faults.

For simplicity, we follow McCaffrey's block model geometry [*McCaffrey*, 2005] outside of the greater Mojave region and substitute its blocks inside the greater Mojave region by several coherent blocks. We use eight blocks with fixed boundaries (SALT, SGOR, SGAB, SMOJ, SWMO, TEHA, INYO, and PANA in Figure 5) in the bordering areas of the Mojave Block and permit variations of the block boundaries within the Mojave Block to consider their effects on the modeling results.

The Mojave Block includes the ECSZ that is a zone of distributed faulting and diffuse shear. Geological studies [e.g., *Oskin et al*., 2008] show the presence of several closely spaced and low slip rate ($\lesssim$2 mm/yr) faults in the Mojave ECSZ, which define the potential block boundaries. Due to the uncertainties in slip rates and fault geometry, uncertainties arise as to the use of mapped surface traces of active faults to define discrete block boundaries, as shown in previous geodetic studies [*McClusky et al*., 2001; *Miller et al*., 2001; *Becker et al*., 2005; *McCaffrey*, 2005; *Meade and Hager*, 2005; *Spinler et al*., 2010; *Loveless and Meade*, 2011; *Johnson*, 2013; *Zeng and Shen*, 2014]. Here the block models within the Mojave Block are objectively crafted on the base of the cluster analysis of the CMM4 GPS velocities rather than subjectively constructed by an arbitrary selection of mapped fault traces as block boundary faults. Nonetheless, the block geometries are allowed to vary as the CMM4 GPS velocities are perturbed by postseismic transients in the epicentral area of the Landers and Hector Mine earthquakes.

The cluster analysis cannot reveal all the details of geological fault boundaries; however, it provides us a first-order definition of potential block boundaries that helps us craft the configuration of fault-aligned block motion models. The *k*-medoids cluster analysis identifies three or four clusters in the CMM4 Mojave GPS data set based on the gap statistics (Figures S11–S13 in the supporting information and Figure 5). We develop a variety of fault-aligned block models following the $k = 3$ and $k = 4$ cluster analyses, respectively (Figure 5).

First, all the block motion models have the easternmost fault boundary along the Ludlow fault, rather than along the Pisgah-Goldstone Lake fault (Figures 5a–5e). While the cluster analysis found a single cluster to the east of the Pisgah-Goldstone Lake fault, we include a block for the region bounded by the Pisgah-Goldstone Lake fault and Ludlow fault because the pre-Landers trilateration data to the east of the Pisgah-Goldstone Lake fault support the inclusion of the Ludlow fault as the easternmost fault boundary.

Second, the region bounded by the Ludlow fault, eastern Garlock fault, Pisgah-Goldstone Lake fault, and eastern Pinto Mountain fault is subdivided into two blocks separated by the Manix-Afton Canyon fault, with the northern one being the NEMD block. Even though the block was not defined in our cluster analysis of the CMM4 velocity field, the subdivision is statistically significant in the reduction of the model misfit to the triangulation and trilateration data with respect to models without the NEMD block. The NEMD block is marked by west-striking left-lateral faults [*Garfunkel*, 1974; *Dokka and Travis*, 1990a, 1990b],

in contrast to other blocks within the Mojave Desert that are cut by northwest trending right-lateral faults, and has been already included in previous model studies [*Johnson*, 2013]. However, comparing to the one in *Johnson* [2013], the western boundary of the NEMD is shifted eastward to the Goldstone Lake fault.

For the two block motion models with four blocks in the Mojave Block (BM3A and BM3B, Figures 5a and 5b), the remaining fault boundary within the Mojave Desert is along the Landers-Camp Rock-Blackwater fault and the Lenwood-Lockhart fault, respectively. For the three block motion models with five blocks in the Mojave Desert (BM4A, BM4B, and BM4C, Figures 5c–5e), two additional faults have to be defined. Model BM4A includes both the Lenwood-Lockhart and Landers-Camp Rock-Blackwater faults (BM4A, Figure 5c). In model BM4B (Figure 5d), the Calico-Blackwater fault is included instead of the Landers-Camp Rock-Blackwater fault used in model BM4A. The two additional block boundaries in model BM4C follow the Calico-Blackwater and Landers-Camp Rock-Lockhart faults (BM4C, Figure 5e). The models BM3B and BM4B are crafted as end-member models without the Landers coseismic rupture in that the clustering of the CMM4 Mojave GPS data may be unable to distinguish the block boundaries in the near field of the Landers earthquake (Figure S13 in the supporting information).

3.2. Block Modeling Approach

Crafting block motion models also requires specification of the kinematic parameters defining block motions. We use translation of rigid blocks plus elastic deformation due to back slip at block boundaries from fault locking to describe the interseismic crustal deformation [*Savage*, 1983]. The amount of slip on the fault boundaries is determined by the relative motion of abutting blocks. The kinematic parameters to be estimated are the block translations (east and north translation rates) of the blocks within the greater Mojave region rather than the commonly used Euler poles [e.g., *McCaffrey*, 2005; *Meade and Hager*, 2005]. That is because geodetic stations in each block do not have enough spatial coverage to simultaneously resolve the position of the rotation pole and the rotation rate; block translation, on the other hand, allows only two parameters for each block, which can be effectively resolved by the data. Block motion of blocks surrounding the greater Mojave region is described by the pertinent Euler poles (longitude and latitude of the rotation pole and rotation rate) as in McCaffrey's block model.

The elastic strain accumulation due to fault locking is calculated using the dislocation model in a homogeneous elastic half space [*Okada*, 1985]. We assume that all the faults that delineate the blocks are vertical, allowing for horizontal fault-parallel and fault-perpendicular (opening/closing) slip vectors. We assign a uniform locking depth of 15.0 km for fault segments following seismological studies [e.g., *Magistrale*, 2002; *Rolandone et al*., 2004], consistent with locking depths used in previous geodetic studies [e.g., *Becker et al*., 2005; *Meade and Hager*, 2005].

3.3. Inversion Method

We use the Bayesian inversion approach [*Fukuda and Johnson*, 2008] to estimate the block translation rates, relative data weights among data sets, and a scaling parameter that places the relative weight on the regularization term of fault-normal rate minimization. The inversion is nonlinear, as the shear strain rates and the corresponding azimuths are nonlinearly related to the block translation rates. Full details about the inversion method are described in Appendix A.

4. Results

Five groups of inversions are explored in this study (Table 1 and Text S4 in the supporting information). Two groups of inversions that consider unequal data weights (Group A and Group B) are carried out with slightly different a priori constraints imposed. In Group A, the relative data weights applied to the triangulation shear strain rates and the corresponding azimuths, rates of EDM line-length change, and far-field GPS velocities are allowed to vary and to be optimally estimated. In Group B, we retain the model setting and data weighting the same as in Group A but set bounds to the strike-slip rates of the southern SAF segments. To further examine the effects of data weight on the modeling results, we consider two additional groups of inversions (Group C and Group D) that apply equal data weight, with parameterizations otherwise the same as the inversions of Group A and Group B, respectively. Finally, we test an inversion constrained by CMM4 GPS velocities alone (Group E, incorporating both the near-field and far-field data; Text S4.5 in the supporting information).

Table 1. Inversion Scenarios

	Data				Weighting	A Priori Constraints
Scenario[a]	Triangulation Data	Trilateration Data	Far-Field GPS	Near-Field GPS	Relative Data Weights	Bounded Southern SAF Dextral Slip Rates
Group A	✓	✓	✓	×	✓	×
Group B	✓	✓	✓	×	✓	✓
Group C	✓	✓	✓	×	×	×
Group D	✓	✓	✓	×	×	✓
Group E	×	×	✓	✓	×	✓

[a]"✓"and "×"indicate "Yes/Considered" and "No/Omitted.

4.1. Unequal Data Weight Model

We start with the Group A inversions that estimate the relative weights among data sets ($\sigma_1^2 \neq \sigma_2^2 \neq \sigma_3^2$) simultaneously with other parameters without bound constraints applied to the strike-slip rate of the southern SAF. For all five block motion models, the predicted strain rates are comparable in magnitude to the observed pre-Landers strain rates provided the uncertainties of the observations (Figure S18 in the supporting information). The model predictions show broadly distributed deformation across the entire Mojave triangulation network extending from the Ludlow fault to the Helendale fault, which differs from the bell-shaped distribution of deformation across the Mojave ECSZ produced by an infinitely long, buried fault zone model used by *Sauber et al*. [1994].

Misfits of the models to the trilateration data are summarized in Table S19 in the supporting information. We visualize the model fit to the trilateration data by computing velocities from the observed rates of line-length using a model coordinate solution [*Segall and Matthews*, 1988] with the modeled trilateration station velocities to constrain the null-space. We find that all the block models capture the first-order pattern of the trilateration data (Figures S19 and S20 in the supporting information).

The residuals of the GPS velocities (observed minus predicted) are shown in Figure S21 in the supporting information. In the far-field, most of the residuals are within the 39% confidence error ellipses (except for those in the block SGAB). The residuals in the block SGAB cannot be reconciled with rigid block motion. In the block SGAB, the residuals reveal fault-normal convergence (southwestward) in the vicinity of the Cucamonga fault, Sierra Madre fault, and San Gabriel fault; however, fault-parallel residuals show northwestward motion in the vicinity of the Mojave SAF. The near-field GPS data are not used in the inversion, but the corresponding residuals are also shown in Figure S21 in the supporting information. The near-field GPS velocity residuals resemble an asymmetric right-lateral shear motion across the Landers-Hector Mine fault zone.

The summed strike-slip rates across the southern and northern Mojave ECSZ are 16.5–17.2 mm/yr and 16.2–18.5 mm/yr, respectively (Figure S21 and Tables S13–S17 in the supporting information). The unmodeled fault-perpendicular motion in the vicinity of the western boundary of the block SGAB (Figure S22 in the supporting information) is associated with the convergence across the Cucamonga and Sierra Madre thrust faults, which are here simplified as anti-dilational vertical dislocations. In spite of such a deficiency of the block models used, the effects of the fault motion of the Cucamonga and Sierra Madre faults are localized and do not have a significant effect on the deformation field in the interior of Mojave.

4.2. Unequal Data Weight and Bounded Slip Rate Model

Next, we examine the extent to which the consideration of the long-term geologic slip rates contributes to the recovery of the secular deformation field within the Mojave. Geologic slip rates on the fault strands of the southern SAF are considered, because elastic strain accumulation of the nearby SAF segments may alter the deformation field within the Mojave [*Snay et al*., 1996; *Savage and Lisowski*, 1998]. The right-lateral slip rate of the Mojave SAF estimated in Group A inversions (ranging from 12.8 to 13.9 mm/yr) is less than half of the geologically determined slip rates of 20–40 mm/yr [e.g., *Weldon et al*., 2002; *Matmon et al*., 2005], and the right-lateral slip rate on the San Bernardino SAF (ranging from 3.5 to 4.2 mm/yr) is lower than the geologic lower bound of 7 mm/yr [e.g., *McGill et al*., 2013]. We prescribe bound constraints to the

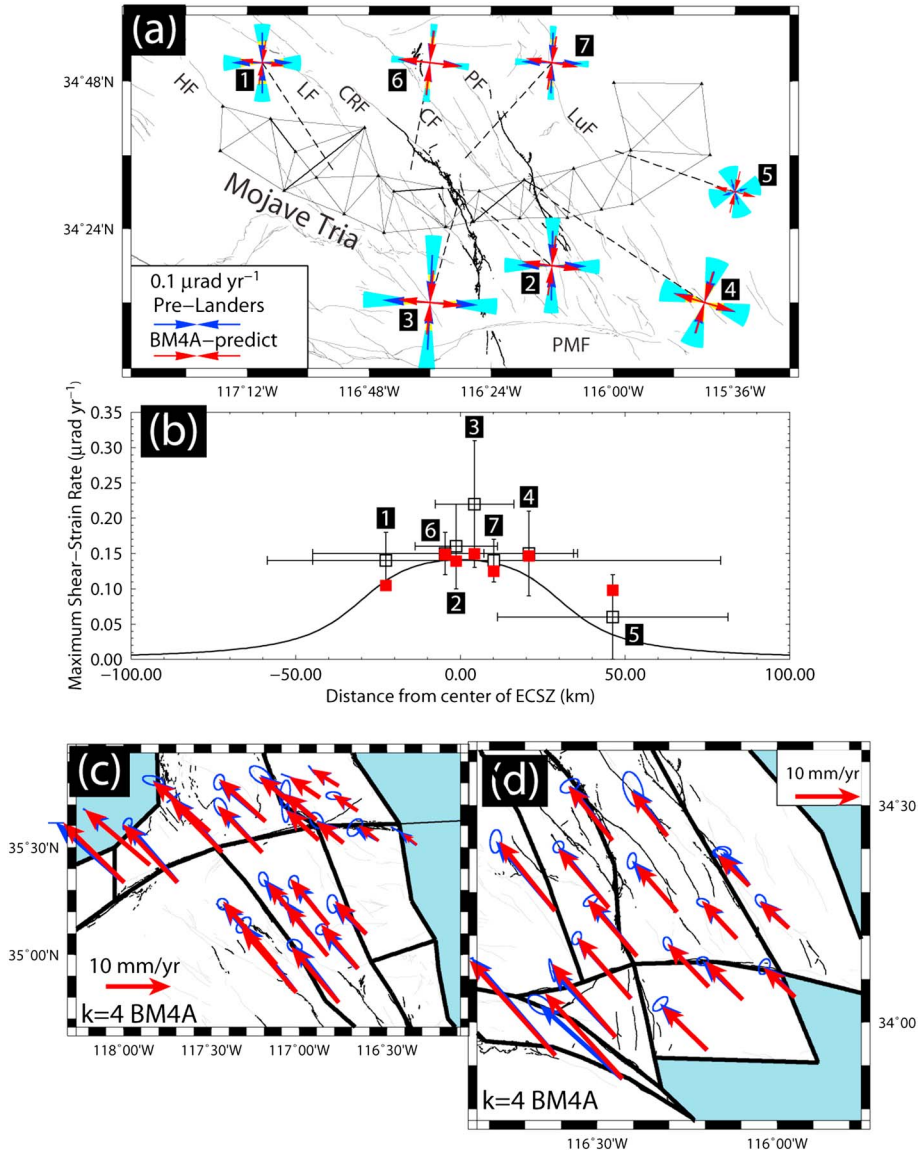

Figure 6. Performance of model BM4A (Group B) in fit to the pre-Landers triangulation data and trilateration data. (a) Pre-Landers observed (blue cross vectors) and predicted (red cross vectors) strain rates, respectively. The fan-shaped sectors in cyan color indicate the one-sigma uncertainties of the principal strain rates, derived from historic observations. The numbers denote the subnetworks labeled in the first column of Table S1 in the supporting information. (b) Strain rate profile across the Mojave ECSZ. The *x* axis is the distance along profile, which is perpendicular to the strike of the shear zone. The vertical axis is the shear strain rate. The open squares and the vertical error bars are the observed maximum shear-strain rates and their one-sigma uncertainties, and the horizontal bars show the geographic spans of the subnetworks. The red squares are the model predicted maximum shear-strain rates for the subnetworks. The solid curve indicates shear strain rates predicted by a distributed shear of 12 mm/yr buried below a locking depth of 15 km across an ~60.0 km wide shear zone. (c) BM4A-derived velocities (red vectors) and model coordinate solution of station velocities (blue vectors) within the Barstow and Garlock networks. (d) BM4A predicted (red vectors) and model coordinate solution derived (blue vectors) station velocities within the Landers and Joshua Tree networks. The model coordinate solution is derived from the observed rates of line-length change with the null parameter space constrained using the BM4A-derived trilateration station velocities. Ellipses at the tip of the velocity vectors represent errors at the 95% confidence. The thick lines show the fault segmented block boundaries.

strike-slip rates of the southern SAF segments as a priori constraints in Group B inversions with the model setting and data weighting the same as in Group A (Table 1). The SAF bifurcates into two segments, namely, the Mission Creek and Banning faults, to the northwest of the Coachella SAF. As the slip partitioning between the Mission Creek and Banning fault strands of SAF is poorly constrained [*Fumal*

et al., 2002; *Yule and Sieh*, 2003; *Behr et al*., 2010], the bound constraint is applied to the sum of the slip rates of the Mission Creek and Banning fault strands. Based on the geologic fault slip rates compiled by the UCERF3 project (UCERF3 (Uniform California Earthquake Rupture Forecast, Version 3) http://pubs.usgs.gov/of/2013/1165/), the bound constraints are set as 20–40 mm/yr on the Mojave SAF [e.g., *Weldon et al*., 2002; *Matmon et al*., 2005], 7–30 mm/yr on the San Bernardino SAF [e.g., *McGill et al*., 2013], 4–30 mm/yr on the Mission Creek plus Banning fault strands [*Fumal et al*., 2002; *Yule and Sieh*, 2003; *Behr et al*., 2010], and 10–30 mm/yr on the Coachella SAF [*van der Woerd et al*., 2006; *Behr et al*., 2010].

These models (except for model BM3B) fit the pre-Landers data better than models in Group A (Figure 6 and Table S21 and Figures S25–S27 in the supporting information), with a reduction of weighted-residual sum of squares by 10%–20%. However, they fit the GPS velocities (Figure 7 and Figure S28 in the supporting information) worse than the corresponding models in Group A (Figure S21 in the supporting information), with an increase of weighted-residual sum of squares by 31%–37%. The larger misfits are mostly due to worse data fitting in the northwestern Mojave and block SGAB. In the other blocks, the magnitudes of GPS velocity residuals are comparable between Group A and Group B. The GPS velocity residuals in the northwestern Mojave are oriented northerly or northwesterly, which differ from the eastward or northeastward GPS velocity residuals in Group A inversions.

The Group B inversions consistently result in a zone of symmetric right-lateral shear in the near-field GPS velocity residuals, irrespective of the different fault-block geometries (Figure 7 and Figure S28 in the supporting information), which differs from the asymmetric right-lateral shear pattern in Group A inversions (Figure S21 in the supporting information).

A comparison of the strike-slip rates between Group A (Figure S21 in the supporting information) and Group B (Figure S28 in the supporting information) reveals slip transfer between the San Gabriel fault, Mojave SAF, and the faults trending northwest within the Mojave (Tables S13–S17 in the supporting information): for all the five block models in Group B, an ~7–8 mm/yr increase of the strike-slip rates across the Mojave SAF (~20.9 ± 0.1 mm/yr) is accommodated by ~4 mm/yr and ~3–4 mm/yr decrease of strike-slip rates across the San Gabriel fault and faults within the Mojave, respectively. The summed strike-slip rates across the southern and northern Mojave ECSZ for Group B models are 13.2–13.7 mm/yr and 13.3–14.4 mm/yr, respectively (Tables S13–S17 in the supporting information).

4.3. Other Block Motion and Fault Slip Models

To explore the effects of data weights, we test two inversion scenarios (Groups C and D) that apply equal data weight and retain the other model settings the same as the Group A and Group B inversions, respectively (Table 1). Details of the two model groups are described in Texts S4.3 and S4.4 in the supporting information. Comparing the modeling results of the four groups, we find that the estimated block translation rates (Tables S8–S12 in the supporting information) and fault slip rates (Tables S13–S17 in the supporting information) are insensitive to whether the relative data weights are assumed the same or optimally estimated in the inversions.

To assess how differently the near-field GPS would contribute, we also test another group of inversion models (Group E) that are constrained by the near-field and far-field CMM4 GPS velocities only (Table 1). Details of the modeling result are in Text S4.5 in the supporting information. Result shows that the summed strike-slip rates across the Mojave ECSZ are consistent with those in Group B inversions but the locus of dextral shear is localized along the Pisgah fault (Figure S43 in the supporting information). A near-field dextral shear also remains in the GPS velocity postfit residuals, but the magnitude of the relative motion attenuates with distance from the fault.

5. Discussion

5.1. Model Discrimination

We find it difficult to choose a preferred block motion model by assessing the slip rates of faults within the Mojave. The summed slip rates across the ECSZ are consistent between the different models, ranging from 16.2 mm/yr to 18.5 mm/yr in Group A and from 13.2 mm/yr to 14.4 mm/yr in Group B. The sparse data used in our experiments cannot resolve the details of slip partitioning within the Mojave Desert, given the presence of narrowly spaced faults slipping at low rates. Furthermore, assessment of the solutions by the

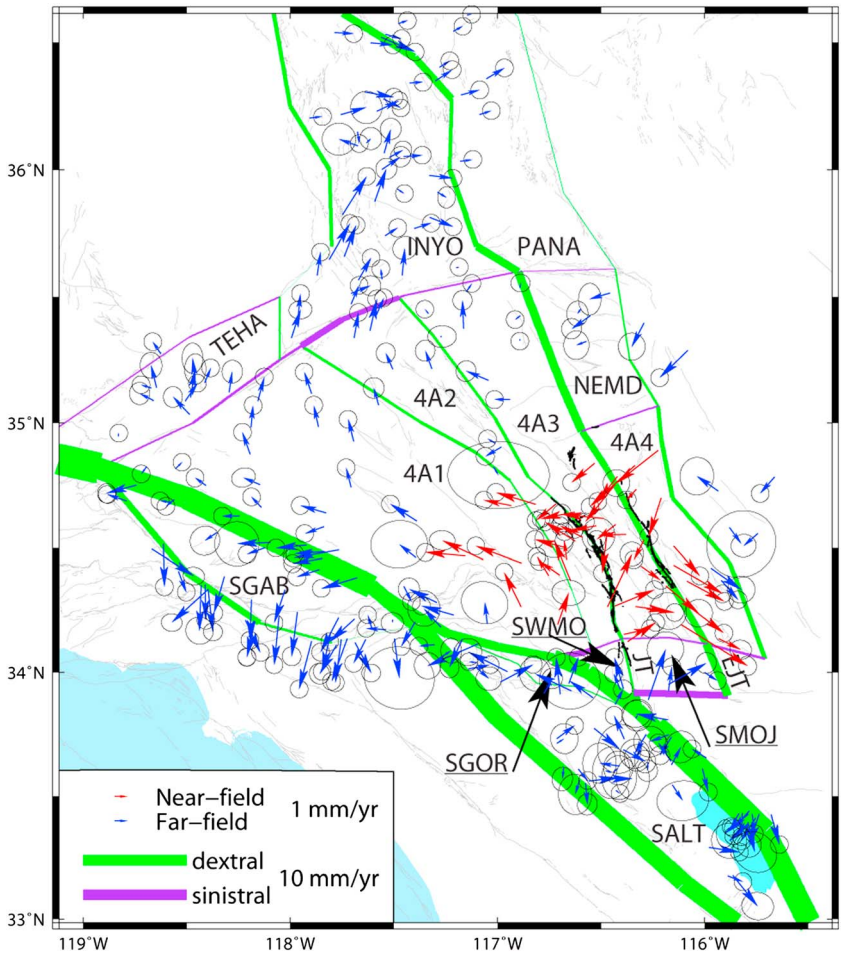

Figure 7. BM4A (Group B) model predicted strike-slip fault slip rates and GPS velocity residuals. The green and purple lines show the right-lateral and left-lateral slip components, respectively, with line widths proportional to the magnitudes of slip rates. The red and blue vectors show the residuals of the near-field and far-field GPS velocities, respectively, with the error ellipses representing the 39.35% confidence. The thick black lines indicate the coseismic ruptures of the Landers and Hector Mine earthquakes. JT: the Joshua Tree fault, EJT: the Eastern Joshua Tree fault.

goodness of fit to data is complex and difficult because of the following reasons. (1) The inverse problem is nonlinear and involves a priori constraints; the classic statistical methods such as *F* test cannot be applied directly because the solution degree of freedom cannot be determined from the inversion result directly [*Jackson and Matsu'ura*, 1985]. (2) The conventional assessment of nonlinear inversion results through evaluation of weighted-residual sum of squares of all the data sets cannot be completely objective because the data sets entered for model constraints cannot all be treated equally, as the far-field GPS velocity data, although more precise than preseismic triangulation/trilateration data, may be affected by Landers-Hector Mine postseismic deformation; such an effect, although perhaps small, is not random and difficult to quantify, therefore cannot be diminished simply by reweighting of the data. For that case, we resort to post-fit weighted-residual sum of squares of the triangulation/trilateration data only to assess the quality of the solutions. This assessment is arguably somewhat subjective, but it quantifies the unbiased modeling and fitting of the preseismic data within the Mojave ECSZ, which is the main focus of this study.

Five block motion models were used to explore the secular deformation field in the Mojave region, and each model was derived in two standard groups of inversions, as described in section 4. Four models in Groups B that apply bounds to the strike-slip rate of the southern SAF yield better data fitting to the pre-Landers data than Group A inversions. The Group B solution is also better than the other three inversion scenarios in the model fit to the pre-Landers data. Therefore, we choose the solutions of Group B in the following discussions.

The models BM4A, BM4B, and BM4C, with one more block included, fit the pre-Landers observations better than do models BM3A and BM3B. The modeled near-field GPS velocities are consistent within 2 mm/yr although the fault geometries vary between the five models in Group B (Figure 7 and Figure S28 in the supporting information). These five block motion models consistently show an excess of the near-field CMM4 GPS velocities in the form of a symmetric right-lateral shear motion near the Landers and Hector Mine earthquake ruptures (Figure 7 and Figure S28 in the supporting information). The preferred model is model BM4A of Group B if we just compare the model fit to the pre-Landers triangulation and trilateration observations (Table S21 in the supporting information).

What deserves further consideration of the modeled deformation field in Group B (except for model BM3A) is that the GPS velocity residuals resemble right-lateral shear across the Blackwater fault with differential fault-parallel velocity of ~1.0 mm/yr across an ~55 km wide northwest trending zone (Figure 7). The inversions based on the CMM4 GPS velocities alone (Group E) absorb such a gentle right-lateral shear and find less than 1.5 mm/y increase of the right-lateral slip rate to 3.3–4.8 mm/yr across the Blackwater fault (Figure S43 and Tables S15–S17 in the supporting information). This suggests that the CMM4 GPS velocities in the northern Mojave may not contain a resolvable contribution from postseismic transients of the two recent Mojave earthquakes. However, a 1992–2000 averaged estimate obtained from interferometric synthetic aperture radar found a 20 km wide zone of concentrated shear along the Blackwater-Little Lake fault system [*Peltzer et al*., 2001]. *Peltzer et al*. [2001] inferred a 7 ± 3 mm/yr slip rate on the Blackwater fault, larger than the 2.7–3.4 mm/yr slip rates derived from the three models in Group B. Their estimate was derived without any attempt to remove the long-term postseismic decay and therefore may contain appreciable postseismic transients.

5.2. Comparison With Other Velocity Fields

We thoroughly compared the BM4A-model derived velocities (Group B) with four other independently derived GPS velocity solutions and two EDM-derived pre-Landers velocity fields (Text S5 in the supporting information). The GPS solutions considered are the USGS near-field GPS velocity field within the Hector Mine monitoring network (http://earthquake.usgs.gov/monitoring/gps/HectorMine/), the Eastern Transverse Ranges to the south of the Pinto Mountain fault and San Bernardino Mountains campaign GPS velocity field [*Spinler et al*., 2010], the PBO velocity solution (ftp://data-out.unavco.org/pub/products/velocity/), and the SOPAC velocity solution (http://sopac.ucsd.edu/dataArchive/). This comparison helps us assess the extent to which postseismic transients are left in the other secular velocity fields and the applicability of the EDM-derived pre-Landers velocity fields.

Our analysis shows that appreciable postseismic transients in the near field of the Landers and Hector Mine coseismic ruptures also exist in the other velocity fields realized from GPS data collected since the 1999 Hector Mine earthquake (Figure 8 and Figures S45–S47 in the supporting information). The excess of the N40°W directed velocity component of the CMM4, PBO, and SOPAC velocity solutions with respect to the BM4A-derived velocities is spatially variable (Figure 8). The 1–3 mm/yr excess of the N40°W directed velocities is uniformly distributed to the west of the Calico fault in the northwestern lobe (profile A–A′, Figure 8b). The 2–4 mm/yr deficit of the N40°W directed velocities is concentrated in the vicinity of the Pisgah fault in the southeastern lobe (profile B–B′, Figure 8b). Our newly derived velocity field, relying on pre-earthquake triangulation and trilateration observations in the Mojave Desert to constrain a block-motion model (BM4A), mitigates most of the near-field postseismic transients evident in the other velocity solutions. This velocity field also agrees within uncertainties with two EDM-derived pre-Landers estimates [*Savage and Svarc*, 1997; *Savage et al*., 2003] in the Landers trilateration network and across the Emerson transect (Figure S48 in the supporting information). However, as we use the far-field GPS to constrain the inversions, it is possible that small postseismic transients may still exist in the far-field GPS velocities, which depends on how far the postseismic transients reach and how effectively they are removed by subtracting a functional representation. A set of Model BM4A (Group B) predicted GPS velocities at the CMM4 sites is provided in Table S28 in the supporting information.

5.3. Slip Partitioning Within the Mojave ECSZ

Using GPS velocities derived from data collected subsequent to the Mojave Desert earthquakes, previous elastic block motion models predicted a range of total Mojave ECSZ slip rates ranging from ~9 mm/yr to

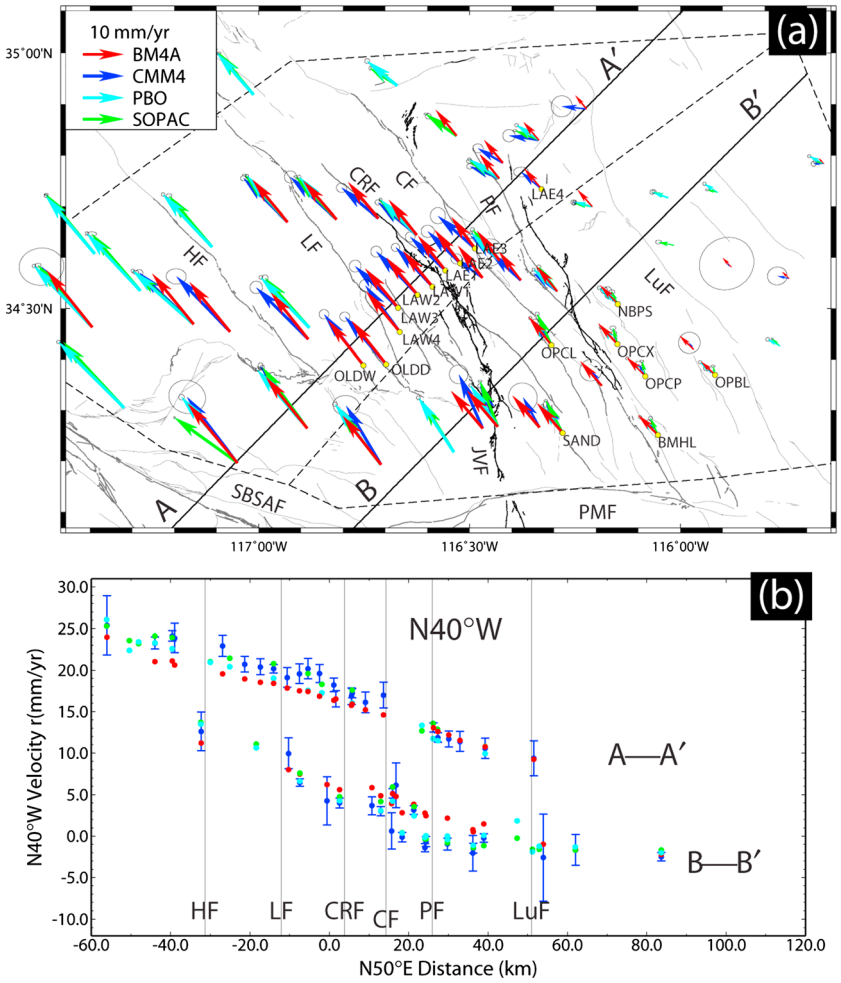

Figure 8. (a) Mapview of near-field velocity fields: CMM4 GPS (blue), Group B BM4A (red), SOPAC GPS (green), and PBO GPS (cyan). The ellipses at the tip of the velocity vectors represent errors at the 95% confidence. The dashed polygons in the northwest and southeast regions delineate the GPS sites whose velocities are plotted at two profiles along the directions of A-A′ and B-B′, respectively. JVF: Johnson Valley fault. (b) N50°E trending station velocity profiles of A-A′ and B-B′ for N40°W directed velocity component (5 mm/yr and −4 mm/yr vertical offsets are added for A-A′ and B-B′ sites). The error bars represent two standard deviations.

~18 mm/yr: ~11.0 ± 2.0 mm/yr [*McClusky et al.*, 2001], ~14.0 mm/yr [*Miller et al.*, 2001], ~13.9 ± 12.0 mm/yr [*Becker et al.*, 2005], 9.3 ± 0.7 mm/yr [*McCaffrey*, 2005], 17.5 ± 1.7 mm/yr [*Meade and Hager*, 2005], 13.6–17.8 mm/yr [*Spinler et al.*, 2010], and 17 mm/yr [*Loveless and Meade*, 2011]. These estimates and those we present in this study are sensitive to the model assumptions made and the fault-block geometries crafted, rendering direct comparisons between models and between different sources (e.g., geodetic versus geologic data constraints) difficult.

In this study, the deformation across the Mojave ECSZ is constrained by the pre-Landers historical geodetic observations and present-day far-field GPS velocities. The internal deformation obtained from the pre-earthquake data within the Mojave ECSZ is more uniformly distributed relative to that reflected in the near-field GPS observations (Figure 8). The GPS velocity solutions biased by remaining postseismic transients (e.g., CMM3, CMM4, PBO, SOPAC, and other velocity solutions) have a sharp velocity gradient across the southern Mojave ECSZ as shown in Figure 8b. A more uniform dextral shear across the southern Mojave ECSZ in our block model-based velocity fields implies more uniform slip partitioning between these closely spaced faults compared to previous studies and similar models constrained by GPS velocities alone (e.g., Group E), in which one or two Mojave ECSZ faults accommodate most of the deformation. *Meade and Hager* [2005] inferred that the Pisgah fault accommodated 13.4 ± 1.0 mm/yr of the 17.5 ± 1.7 mm/yr cumulative dextral slip.

Loveless and Meade [2011] inferred that the Landers fault and Pisgah fault accommodated 6 mm/yr and 7 mm/yr of the 17 mm/yr cumulative dextral slip. The Pisgah fault accommodates 60%–85% of the cumulative dextral motion across the Mojave ECSZ in Group E models (Tables S13–S17 in the supporting information).

Independent of elastic model assumptions and uncertainties, geodetic estimates of slip rate across the Mojave ECSZ exceed the Pleistocene slip rate [*Oskin et al*., 2008]. The 13.2 ± 2.3 mm/yr cumulative strike-slip rate across the southern Mojave ECSZ in model BM4A (Group B, Table S15 in the supporting information) roughly agrees with that inferred in previous estimates based on the pre-Landers measurements alone (~8–12 mm/yr) [*Savage et al*., 1990; *Sauber et al*., 1994]. It is in the middle of the slip rates derived by previous elastic block models and is roughly twice the cumulative late Pleistocene slip rate estimates for faults across the southern Mojave (≤6.2 ± 1.9 mm/yr) [*Oskin et al*., 2008]. There are several low-slip-rate active faults in the northern Mojave (maximum geologic slip rate ≤ ~1.0 mm/yr), such as the Gravel Hills, Lockhart, Blackwater, Paradise, and Goldstone Lake faults (UCERF3, http://pubs.usgs.gov/of/2013/1165/). The 14.4 ± 1.6 mm/yr cumulative slip rate across the northern Mojave ECSZ (Group B, Table S15 in the supporting information) is at least twice the geologic cumulative slip rate. Furthermore, the right-lateral slip rate across the Blackwater fault is 2.7–4.5 mm/yr (Tables S13 and S15–S17 in the supporting information) in Group B inversions, which is significantly larger than geologic slip rate of 0.49 ± 0.04 mm/yr [*Oskin and Iriondo*, 2004].

The elastic deformation from the nearby Mojave and San Bernardino SAF likely affects the deformation field within the Mojave. The dextral slip rates across the Mojave and San Bernardino SAF derived in model BM4A (Group B, Table S15 in the supporting information) are 20.9 ± 0.1 mm/yr and 8.4 ± 0.6 mm/yr, consistent with the lower bound from the latest Pleistocene SAF slip rate estimates (UCERF3). Had the dextral slip rate across the San Bernardino SAF been raised up to at least 15 mm/yr in Group B inversions (the lower bound of San Bernardino SAF dextral slip rate is set to the geologic slip rate estimate of 15 mm/yr), the Mojave ECSZ cumulative slip rate would decrease by approximately 1 mm/yr, and the model fit to the pre-Landers triangulation and trilateration data (weighted-residual sum of squares) is reduced by ~20% with respect to Group B inversions, but the near-field right-lateral shear pattern in the GPS velocity residuals remain. Although several previous geodetic studies with geologic rates as additional constraint inferred 13–17 mm/yr dextral slip rate across the San Bernardino SAF [e.g., *Bird*, 2009; *Zeng and Shen*, 2014], we still choose the lower geologic slip rate bound being 7 mm/yr in Group B inversions. The pre-Landers historical geodetic data favor San Bernardino SAF slip rates near the lower bound in our elastic block motion models. The estimated slip rates may be lower than the long-term slip rate due to the effect of enduring postseismic transients of the 1857 M_w 7.9 Great Fort Tejon earthquake [*Hearn et al*., 2013].

The external constraints on the distribution of deformation within the Mojave from the far-field GPS velocities are consistent with those used in some previous elastic block modeling. With the additional constraints from pre-Landers historical geodetic data and a priori southern SAF slip rate (Group B, Table 1 and Tables S13–S17 in the supporting information), the cumulative slip rates across the southern Mojave ECSZ are ~4 mm/yr lower than the slip rates in models assuming roughly the same shear zone width [e.g., *Meade and Hager*, 2005; *Spinler et al*., 2010; *Loveless and Meade*, 2011]. It is noteworthy that our cumulative deformation is consistent with that derived from a block model constrained by both GPS velocities and pre-Landers stress-orientation data at seismogenic depths [e.g., *Becker et al*., 2005]. The cumulative slip rates across the southern Mojave ECSZ are ~4 mm/yr larger than that derived from block models that allow internal straining of blocks [e.g., *McCaffrey*, 2005]. Some of the previous block models [e.g., *McClusky et al*., 2001; *Miller et al*., 2001] used the GPS velocities mostly north of ~34.7°N latitude and found cumulative slip rates across the northern Mojave ECSZ consistent with Group B slip rates (e.g., BM4A-derived 14.4 ± 1.6 mm/yr).

Several mechanisms have been invoked to interpret the geologic-geodetic slip rate discrepancy in the southern Mojave ECSZ (Text S6 in the supporting information), including earthquake cycle effects [*Chuang and Johnson*, 2011; *Johnson*, 2013], long-range fault interactions [*Dolan et al*., 2007], transient weakening of a ductile shear zone at depth [*Oskin et al*., 2008], and off-fault deformation [*Herbert et al*., 2013, 2014]. Our block motion models cannot discriminate between these candidate mechanisms, as we do not consider earthquake cycle effects or evolution of fault zone rheology, and we do not attempt to solve for distributed off-fault deformation.

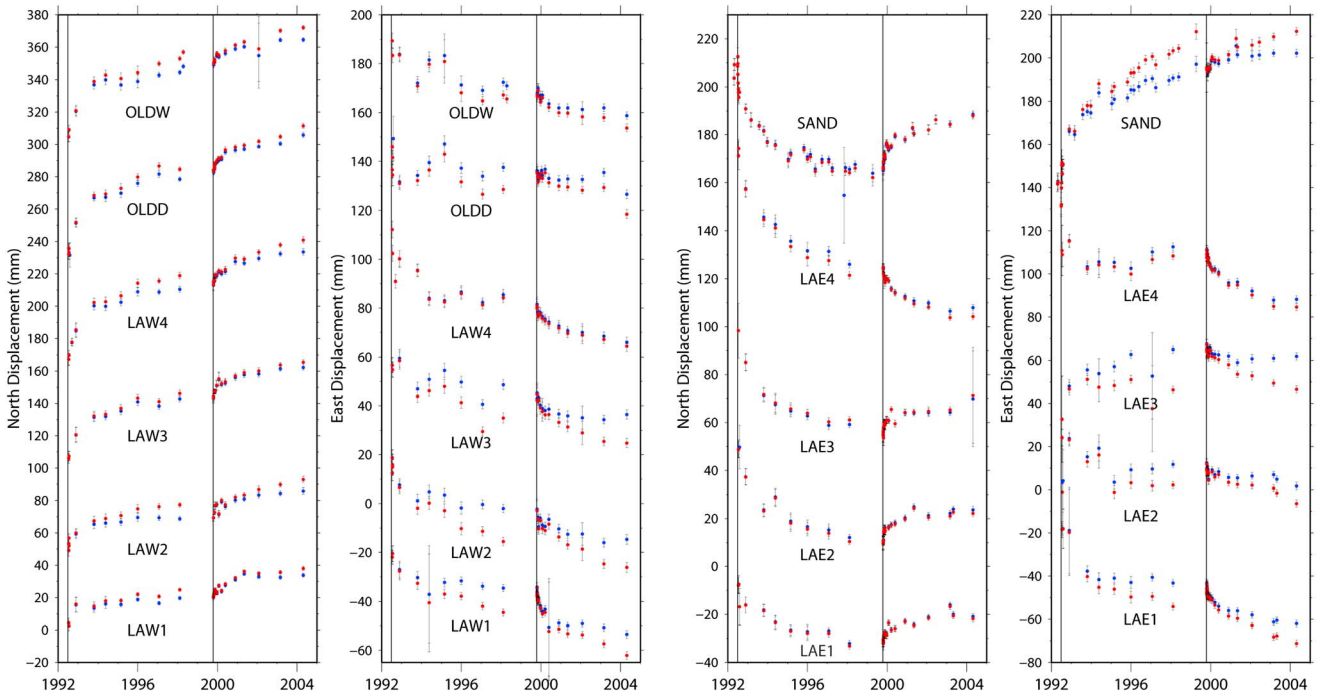

Figure 9. Postseismic GPS displacement time series (less a nominal constant) of the USGS Emerson Transect for sites located (a) west and (b) east of the Landers rupture based on the raw CMM4 time series. The blue dots are corrected for the CMM4 estimate of interseismic velocities, and the red dots are reduced by the BM4A-derived velocities. Coseismic offsets by the Hector Mine earthquake marked by vertical black lines are removed. The left column shows the north component, and the right column shows the east component, respectively. The error bars are one-sigma formal error from the CMM4 time series data. One-sigma uncertainties greater than 20 mm are reduced to 20 mm.

5.4. Implications for Near-field Postseismic Deformation

We test the effects of using different realizations of the interseismic velocity fields on estimates of postseismic GPS time series of stations near the Landers and Hector Mine ruptures (details are in Text S7 in the supporting information). The BM4A-based postseismic time series show several millimeters to nearly 20 mm greater cumulative displacements than the CMM4-derived estimates of postseismic motions for stations along the USGS Emerson transect, both during the time period between the two earthquakes and in the 5 years after the Hector Mine earthquake (Figure 9). For the sites located in the southeastern Mojave, where the differences in velocity field realizations with and without preseismic data are greatest, the BM4A-based postseismic time series show more prominent and enduring late-stage transient motions in the first decade following the Hector Mine earthquake than the time series reduced by their PBO-based velocity estimates (Figures 8 and 10).

A comparison of the cumulative postseismic-only displacement estimates over three time intervals is shown in Figure 11. The BM4A-based post-Landers displacements from 1992 to 1999 agree within uncertainties with the CMM4-based postseismic displacements but appear systematically larger at many sites (Figure 11a). The cumulative displacements derived from the BM4A-based post-Hector Mine time series differ from those derived from the October 1999 to 2004 CMM4-based (Figure 11b) and the 2004 to 2010 PBO-based (Figure 11c) postseismic relaxation time series. The BM4A-based 2004–2010 postseismic displacements indicate substantial continued motions in the southeastern Mojave, while the PBO-based postseismic displacements are smaller.

If the estimates of secular velocities used in postseismic modeling studies are biased, so will be the inferences regarding the rheological structure and the fault zone properties inferred from the postseismic relaxation signals. The additional shear motion in the BM4A-referenced postseismic time series implies faster and more enduring postseismic motions in the near field of the Landers and Hector Mine earthquakes. In turn, this may suggest that the lower crust was flowing more or that a ductile shear zone at depth was creeping faster in the first decade after the Hector Mine earthquake than previously inferred.

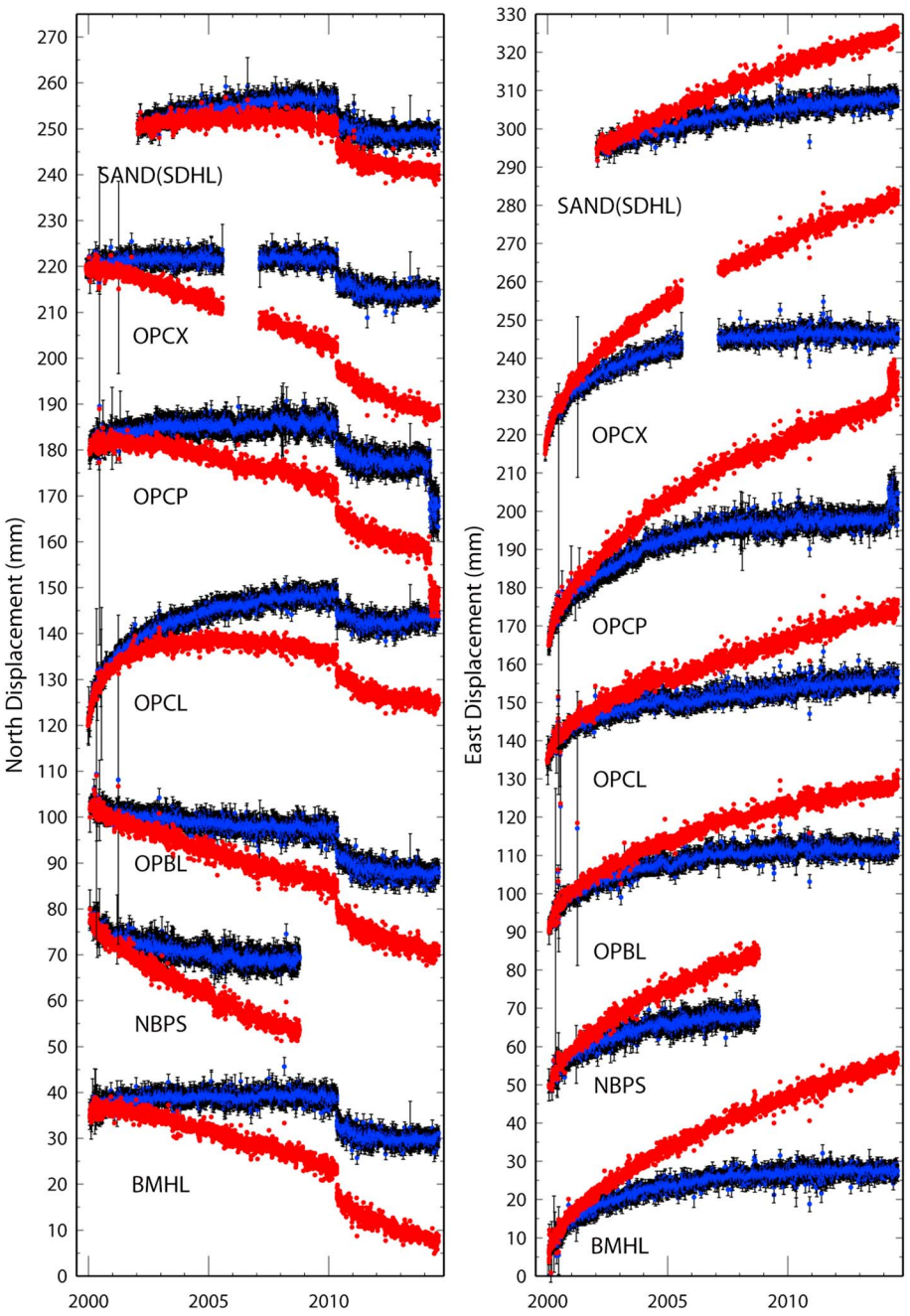

Figure 10. Postseismic GPS time series (less a nominal constant) of GPS sites in the southeastern Mojave based on raw PBO time series data. Blue dots: less the interseismic velocity estimate from the PBO solution, and red dots: less the BM4A-predicted velocities. The left and right columns show the north and east components, respectively. The error bars are one-sigma standard deviations from the PBO time series.

6. Conclusions

The Landers and Hector Mine earthquakes altered the deformation field in the Mojave Desert, which adversely affects the use of GPS observations to estimate the secular deformation field (interseismic deformation just prior to the recent earthquakes) in the epicentral area of the Landers and Hector Mine earthquakes. We use block motion models constrained by both historical pre-Landers triangulation/trilateration observations and post-Landers GPS velocity estimates potentially corrected for postseismic contributions to recover the secular deformation field in the Mojave Desert (Table S28 in the supporting information), especially in the

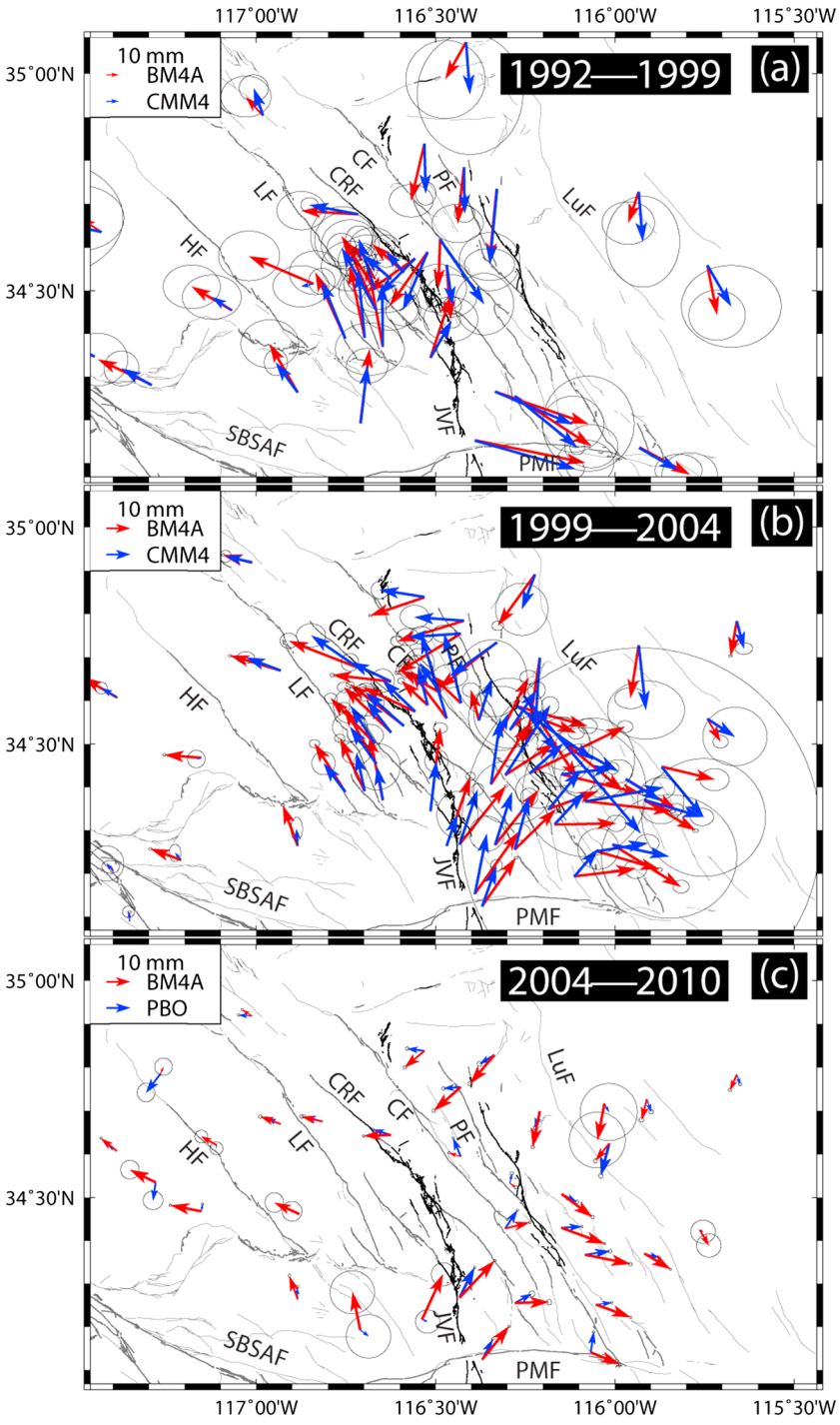

Figure 11. Postseismic displacements in the time spans of (a) post-Landers–Hector Mine, (b) post-Hector Mine–2004.0, and (c) 2004.0–2010.3. The blue and red vectors in Figures 11a and 11b are the CMM4 station displacements less the CMM4 estimated velocity contributions and the BM4A predicted velocity contributions, respectively. The blue and red vectors in Figure 11c are the PBO station displacements less the PBO estimated velocity contributions and the BM4A predicted velocity contributions, respectively.

near field of the rupture zones of earthquakes. The CMM4, PBO, and SOPAC GPS velocity field realizations appear to contain residual postseismic transients in the form of an excess right-lateral shear motion in the near field of the Landers and Hector Mine earthquakes, which are mitigated in the secular velocity field derived by our study.

Independent of elastic model assumptions and uncertainties, geodetic estimates of slip across the Mojave ECSZ greatly exceed the Pleistocene fault slip rate estimates. The cumulative fault slip rates are 13.2 ± 2.3 mm/yr and 14.4 ± 1.6 mm/yr, respectively, across the southern and northern Mojave ECSZ in the preferred block motion model. Models that incorporate contributions from off-fault deformation and viscoelastic relaxation of the lower crust and upper mantle appear to be able to reconcile the discrepancy of geologic and geodetic estimates. As the slip rates are along-strike averages, future models should also pay special attention to along-strike segmented deformation as shown in *Zeng and Shen* [2014].

Postseismic GPS time series of the Landers and Hector Mine earthquakes based on our secular velocity field reveal enduring late-stage transient motions in the near field of the coseismic ruptures that should provide new constraints on the rheology of the lower crust.

Appendix A: Inversion Method

Let $\mathbf{v}$ be an $N\times 1$ dimensional vector of N_s stations' modeled surface velocities ($N=2N_s$). We define an $M\times 1$ dimensional vector $\mathbf{m}$ of M_b blocks' translation rates ($M=2M_b$). Vector $\boldsymbol{\Omega}^0$ denotes Euler poles of blocks outside the greater Mojave region, which is related to $\mathbf{v}$ through a matrix of assembly of site position vectors ($\mathbf{R}$) and a matrix ($\mathbf{E_{EN}}$) that rotate the velocity vectors from the spherical coordinate system to the regional east-north coordinate system, if the stations are also located outside the greater Mojave region. The surface velocities are related to the block motions as follows:

$$\mathbf{v} = \mathbf{B}_T \cdot \mathbf{m} + \mathbf{B}_R \cdot \mathbf{E}_{EN} \cdot \left(\boldsymbol{\Omega}^0 \times \mathbf{R}\right) - \mathbf{G}_F \cdot \mathbf{s}\left(\mathbf{m}, \boldsymbol{\Omega}^0\right) + \boldsymbol{\varepsilon} \tag{A1}$$

where $\mathbf{B}_\mathrm{T}$ and $\mathbf{B}_\mathrm{R}$ are two index matrices that determine whether the translation rates, $\mathbf{m}$, or the Euler poles from McCaffrey's block model, $\boldsymbol{\Omega}^0$, contribute to the velocity components; $\mathbf{G}_F$ contains the Green's functions [*Okada*, 1985] that relate the fault slip rates, $\mathbf{s}(\mathbf{m}, \boldsymbol{\Omega}^0)$, determined by the block motions of abutting blocks and fault geometries, to the predicted surface velocities; and $\boldsymbol{\varepsilon}$ is a vector of data errors.

We assume that the observed and modeled data are related through the following equation:

$$\mathbf{d}_k^\mathrm{o} = \mathbf{d}_k^\mathrm{p}(\mathbf{m}) + \boldsymbol{\varepsilon}_k \quad k = 1, 2, 3 \tag{A2}$$

where $\mathbf{d}_k^\mathrm{o}$ are the data vector of the shear strain rates and the corresponding azimuths ($k=1$), rates of line-length change ($k=2$), and far-field GPS velocities ($k=3$); $\mathbf{d}_k^\mathrm{p}(\mathbf{m})$ are the corresponding model predictions; and $\boldsymbol{\varepsilon}_k$ follows a normal distribution with zero mean and covariance matrix $\sigma_k^2\boldsymbol{\Sigma}_k$ with the σ_k^2 being a scaling factor that controls the relative weights among three data sets and the $\boldsymbol{\Sigma}_k$ being the covariance matrix of the original data, $\mathbf{d}_k^\mathrm{o}$.

We further assume that all the data sets are independent from each other, and we do not consider correlations in the CMM4 GPS velocities. The probability density representation of equation (A2) is

$$p\left(\mathbf{d}_1^\mathrm{o}, \mathbf{d}_2^\mathrm{o}, \mathbf{d}_3^\mathrm{o} | \sigma_1^2, \sigma_2^2, \sigma_3^2, \mathbf{m}\right) = \prod_{k=1}^{3}\left\{\left(2\pi\sigma_k^2\right)^{-N_k/2}|\boldsymbol{\Sigma}_k|^{-1/2}\exp\left[\frac{1}{\sigma_k^2}\left(\mathbf{d}_k^\mathrm{o} - \mathbf{d}_k^\mathrm{p}(\mathbf{m})\right)^\mathrm{T}\boldsymbol{\Sigma}_k^{-1}\left(\mathbf{d}_k^\mathrm{o} - \mathbf{d}_k^\mathrm{p}(\mathbf{m})\right)\right]\right\} \tag{A3}$$

which is also called the likelihood function.

We define the $N_1\times 1$ dimensional vector $\mathbf{d}_1^\mathrm{p}(\mathbf{m}) = [\tau_1{}^\mathrm{p}, \Psi_1{}^\mathrm{p}, \tau_2{}^\mathrm{p}, \Psi_2{}^\mathrm{p}, \ldots, \tau_{Nt}{}^\mathrm{p}, \Psi_{Nt}{}^\mathrm{p}]^T$, the $N_2\times 1$ dimensional vector $\mathbf{d}_2^\mathrm{p}(\mathbf{m}) = [dL_1, dL_2, \ldots, dL_{N2}]^T$ and the $N_3\times 1$ dimensional vector $\mathbf{d}_3^\mathrm{p}(\mathbf{m}) = [ve_1, vn_1, \ldots, ve_{Ng}, vn_{Ng}]^T$ as the model prediction of the maximum shear-strain rates and the corresponding azimuths of N_t triangulation networks ($N_1 = 2N_t$), rates of line-length change of N_2 baselines, and far-field GPS velocities of N_g stations ($N_3 = 2N_g$), respectively.

Following equation (A1), far-field GPS velocities can be derived from a specific block motion model. The maximum shear-strain rates and the corresponding azimuths, together with the rates of line-length change are obtained from the model prediction of surface velocities.

The maximum shear-strain rate, τ_i^p, and its azimuth, Ψ_i^p, of the ith network are derived from the elastic strain rate tensor, $\boldsymbol{\varepsilon}_{ij}$ ($i,j = 1,2$):

$$\tau_i^p = \sqrt{\frac{(\boldsymbol{\varepsilon}_{11} - \boldsymbol{\varepsilon}_{22})^2}{4} + \boldsymbol{\varepsilon}_{12}^2}$$
$$\Psi_i^p = \frac{1}{2}\arctan\left(\frac{\boldsymbol{\varepsilon}_{11} - \boldsymbol{\varepsilon}_{22}}{2\boldsymbol{\varepsilon}_{12}}\right) \tag{A4}$$

where $\boldsymbol{\varepsilon}_{ij}$ are derived from the velocities of at least three sites used to compute the observed strain rates of the triangulation sub network assuming uniform strain rate in the network:

$$V_e^p = a + \boldsymbol{\varepsilon}_{11}x + \boldsymbol{\varepsilon}_{12}y - \omega y$$
$$V_n^p = b + \boldsymbol{\varepsilon}_{12}x + \boldsymbol{\varepsilon}_{22}y + \omega x \tag{A5}$$

where V_e^p and V_n^p are the predicted east and north velocity components of a site, x and y are the east and north coordinates relative to the center of mass of the network, ω is the rotation rate, a and b represent the translation rates. The parameters on the right-hand side of equation (A5) are estimated using least squares, in which we ignore the uncertainties of the data (velocities predicted by the block motion model).

The rate of line-length change, dL_i, of the ith baseline can be expressed as

$$dL_i = \cos\theta(Ve_2 - Ve_1) + \sin\theta(Vn_2 - Vn_1) \tag{A6}$$

where (Ve_1, Vn_1) and (Ve_2, Vn_2) are the velocity vectors of a baseline with the start and end points indicated by the subscripts 1 and 2, θ is the angle measured anticlockwise from the due east.

The optimal solution of the translation vector, **m**, is found by minimization of the following objective function:

$$\Phi(\sigma_1^2, \sigma_2^2, \sigma_3^2, \alpha^2, \mathbf{m}) = \sum_{k=1}^{3} \frac{1}{\sigma_k^2}\left(\mathbf{d}_k^o - \mathbf{d}_k^p(\mathbf{m})\right)^T \boldsymbol{\Sigma}_k^{-1}\left(\mathbf{d}_k^o - \mathbf{d}_k^p(\mathbf{m})\right) + \frac{1}{\alpha^2}(\mathbf{L}\cdot\mathbf{sn})^T(\mathbf{L}\cdot\mathbf{sn}) \tag{A7}$$

where **sn** is the fault-normal slip rate vector of fault segments (except for the southern and western boundaries of the block SGAB and the White Wolf fault), **L** is a diagonal matrix with the diagonal elements being the fault segment length, and α^2 places the relative weight on the regularization term of fault-normal rate minimization.

It is noteworthy that the translation rate vector, **m**, is linearly related to fault-normal slip rate vector, **sn**, through matrix **D** that depends on the fault-block topology and matrix **P** that depends on the fault geometries.

$$\mathbf{sn} = \mathbf{P}\cdot\mathbf{D}\cdot\mathbf{m} \tag{A8}$$

Therefore, the fault-normal rate minimization is equivalent to applying constraints to the translation rate vector.

The fault-normal slip rate minimization is applied because (1) most of the regional faults are predominantly pure strike-slip faults; (2) the inversion otherwise yields a severely "checkerboarding" pattern of alternating fault-normal opening and closing deformation among faults within the Mojave Desert: the geodetic data resolve the summed fault-normal slip rates well, but the data fail to determine the details of fault-normal slip partitioning among spatially close faults [*d'Alessio et al.*, 2005; *Meade and Hager*, 2005]. However, active thrust faults such as the White Wolf fault and the faults in the San Gabriel range front (the Cucamonga fault, Sierra Madre fault, and San Gabriel fault) are excluded from the fault-normal minimization.

In addition to the regularization priors, we found that it is necessary to introduce other prior information on translation rates to stabilize the problem. We prescribe sinistral slip on the Pinto Mountain fault, Garlock fault, and White Wolf fault and dextral motions on the other faults to prohibit unreasonable models, which is equivalent to applying inequality constraints to the translation rates. We also prescribe bound constraints to the dextral slip rates on the SAF from the Mojave to Coachella segments for some of the models (section 4.2, Unequal Data Weight and Bounded Slip Rate Model).

We use the Bayesian inversion approach to combine prior information with the likelihood function to yield the posterior probability distribution function (PDF). The posterior PDF of the parameters

$p(\sigma_1^2, \sigma_2^2, \sigma_3^2, \alpha^2, \mathbf{m}|\mathbf{d_1^o}, \mathbf{d_2^o}, \mathbf{d_3^o})$ is an update of the prior PDF $p(\sigma_1^2, \sigma_2^2, \sigma_3^2, \alpha^2, \mathbf{m})$, with observations represented by the likelihood function $p(\mathbf{d_1^o}, \mathbf{d_2^o}, \mathbf{d_3^o}|\sigma_1^2, \sigma_2^2, \sigma_3^2, \alpha^2, \mathbf{m})$:

$$p(\sigma_1^2, \sigma_2^2, \sigma_3^2, \alpha^2, \mathbf{m}|\mathbf{d_1^o}, \mathbf{d_2^o}, \mathbf{d_3^o}) \propto p(\mathbf{d_1^o}, \mathbf{d_2^o}, \mathbf{d_3^o}|\sigma_1^2, \sigma_2^2, \sigma_3^2, \alpha^2, \mathbf{m}) p(\sigma_1^2, \sigma_2^2, \sigma_3^2, \alpha^2, \mathbf{m}) \tag{A9}$$

The likelihood function $p(\mathbf{d_1^o}, \mathbf{d_2^o}, \mathbf{d_3^o}|\sigma_1^2, \sigma_2^2, \sigma_3^2, \alpha^2, \mathbf{m})$ is independent of α^2; therefore, $p(\mathbf{d_1^o}, \mathbf{d_2^o}, \mathbf{d_3^o}|\sigma_1^2, \sigma_2^2, \sigma_3^2, \alpha^2, \mathbf{m}) \propto p(\mathbf{d_1^o}, \mathbf{d_2^o}, \mathbf{d_3^o}|\sigma_1^2, \sigma_2^2, \sigma_3^2, \mathbf{m})$. The prior PDF $p(\sigma_1^2, \sigma_2^2, \sigma_3^2, \alpha^2, \mathbf{m})$ can be expressed as $p(\sigma_1^2, \sigma_2^2, \sigma_3^2, \alpha^2) p(\mathbf{m}|\alpha^2) p_b(\mathbf{m})$, in which $p(\mathbf{m}|\alpha^2)$ and $p_b(\mathbf{m})$ are probability density representations of the regularization and bound constraint, respectively, and $p(\sigma_1^2, \sigma_2^2, \sigma_3^2, \alpha^2)$ is a uniform PDF.

If the inequality constraints (sinistral or dextral slip for respective fault) are also applied, the posterior PDF is

$$p(\sigma_1^2, \sigma_2^2, \sigma_3^2, \alpha^2, \mathbf{m}|\mathbf{d_1^o}, \mathbf{d_2^o}, \mathbf{d_3^o}) = \begin{cases} \frac{1}{Z}\left[\prod_{k=1}^{3} (\sigma_k^2)^{-N_k/2}\right] (\alpha^2)^{-M/2} \exp\left[-\frac{1}{2}\Phi(\sigma_1^2, \sigma_2^2, \sigma_3^2, \alpha^2, \mathbf{m})\right] p_b(\mathbf{m}) & \text{for } \sigma_1^2 > 0, \sigma_2^2 > 0, \sigma_3^2 > 0, \alpha^2 > 0, \\ & \text{and with correct sense of slip} \\ 0 & \text{otherwise} \end{cases} \tag{A10}$$

where Z is a constant to normalize the distribution.

The shear strain rates and the corresponding azimuths are nonlinearly related to the block translation rates, and $\sigma_1^2, \sigma_2^2, \sigma_3^2$, and α^2 as unknowns, are nonlinear in the prior PDF distributions function. Because the posterior PDF distribution is non-Gaussian, we cannot obtain a closed-form analytical expression of the posterior PDF and instead use the Markov chain Monte Carlo method to get a discrete representation of the posterior PDF [*Fukuda and Johnson*, 2008]. A further analysis of the samples generates the means, formal standard deviations, and 95% confidence intervals of each element of the translation vectors.

To obtain the optimal model parameters and their statistics, we discard the first 1.0×10^5 samples to avoid the impacts of initial assignment of parameters and retain samples every 1000 steps in the next 2.0×10^5 samples of the posterior PDF. Experiments show that the number of samples in these two steps is sufficient to explore the posterior PDF. We also test a series of experiments to choose a suitable step size to explore the model space.

Acknowledgments

We thank J.C. Savage and an anonymous reviewer for their constructive reviews that helped improve and shorten this paper. We also thank Editor Paul Tregoning and Associate Editor Mike Poland for their comments. We appreciate the access to computing resources of the Computer Network Information Center at the Institute of Geology, China Earthquake Administration. This work was partially funded by the National Natural Science Foundation of China (41090294) and by an NSF I/RD grant (EAR-1323052) for the corresponding author as a rotator program director at NSF. Any opinion, findings, and conclusions or recommendations expressed in this material are those of the author(s) and do not necessarily reflect the views of the National Science Foundation. All the figures were generated using the Generic Mapping Tools [*Wessel and Smith*, 1998]. All the data used in this study are in public domain; their sources are provided as references and/or as URLs cited in the text and in the following. The original electro-optical distance measurement (EDM) data in the Landers, Joshua Tree, Barstow, and Garlock networks are at http://earthquake.usgs.gov/monitoring/deformation/geodolite/. The USGS near-field GPS time series of sites within the Hector Mine monitoring network is from http://earthquake.usgs.gov/monitoring/gps/HectorMine/. The PBO velocity solution and position time series are from ftp://data-out.unavco.org/pub/products/ (produced November 26 2014 in the Stable North America Reference Frame, and last accessed 28 December 2014). The SOPAC velocity solution is from http://sopac.ucsd.edu/dataArchive/ (last accessed 28 December 2014). Southern California Earthquake Center publication no. 2087.

References

Becker, T. W., J. L. Hardebeck, and G. Anderson (2005), Constraints on fault slip rates of the Southern California plate boundary from GPS velocity and stress inversions, *Geophys. J. Int.*, *160*(2), 634–650, doi:10.1111/j.1365-246X.2004.02528.x.

Behr, W. M., et al. (2010), Uncertainties in slip-rate estimates for the Mission Creek strand of the southern San Andreas fault at Biskra Palms Oasis, Southern California, *Geol. Soc. Am. Bull.*, doi:10.1130/b30020.1.

Bird, P. (2009), Long-term fault slip rates, distributed deformation rates, and forecast of seismicity in the western United States from joint fitting of community geologic, geodetic, and stress direction data sets, *J. Geophys. Res.*, *114*, B11403, doi:10.1029/2009JB006317.

Bürgmann, R., and G. Dresen (2008), Rheology of the lower crust and upper mantle: Evidence from rock mechanics, geodesy, and field observations, *Annu. Rev. Earth Planet. Sci.*, *36*(1), 531–567, doi:10.1146/annurev.earth.36.031207.124326.

Chuang, R. Y., and K. M. Johnson (2011), Reconciling geologic and geodetic model fault slip-rate discrepancies in Southern California: Consideration of nonsteady mantle flow and lower crustal fault creep, *Geology*, doi:10.1130/g32120.1.

d'Alessio, M. A., I. A. Johanson, R. Bürgmann, D. A. Schmidt, and M. H. Murray (2005), Slicing up the San Francisco Bay Area: Block kinematics and fault slip rates from GPS-derived surface velocities, *J. Geophys. Res.*, *110*, B06403, doi:10.1029/2004JB003496.

DeMets, C., R. G. Gordon, D. F. Argus, and S. Stein (1994), Effect of recent revisions to the geomagnetic reversal time scale on estimates of current plate motions, *Geophys. Res. Lett.*, *21*(20), 2191–2194, doi:10.1029/94GL02118.

Deng, J., M. Gurnis, H. Kanamori, and E. Hauksson (1998), Viscoelastic flow in the lower crust after the 1992 Landers, California, Earthquake, *Science*, *282*(5394), 1689–1692, doi:10.1126/science.282.5394.1689.

Dokka, R. K., and C. J. Travis (1990a), Late Cenozoic strike-slip faulting in the Mojave Desert, California, *Tectonics*, *9*(2), 311–340, doi:10.1029/TC009i002p00311.

Dokka, R. K., and C. J. Travis (1990b), Role of the eastern California shear zone in accommodating Pacific-North American plate motion, *Geophys. Res. Lett.*, *17*(9), 1323–1326, doi:10.1029/GL017i009p01323.

Dolan, J. F., D. D. Bowman, and C. G. Sammis (2007), Long-range and long-term fault interactions in Southern California, *Geology*, *35*(9), 855–858, doi:10.1130/g23789a.1.

Ellsworth, W. L. (1990), Earthquake history, 1769–1989, in *The San Andreas Fault System, California*, *U.S. Geol. Surv. Profess. Pap.*, vol. 1515, edited by R. Wallace, pp. 153–188, U.S. Gov. Print. Off., Washington, D. C.

Fialko, Y. (2004), Evidence of fluid-filled upper crust from observations of postseismic deformation due to the 1992 M_w7.3 Landers earthquake, *J. Geophys. Res.*, *109*, B08401, doi:10.1029/2004JB002985.

Freed, A. M., and R. Burgmann (2004), Evidence of power-law flow in the Mojave desert mantle, *Nature*, *430*(6999), 548–551.

Freed, A. M., R. Bürgmann, and T. Herring (2007), Far-reaching transient motions after Mojave earthquakes require broad mantle flow beneath a strong crust, *Geophys. Res. Lett.*, *34*, L19302, doi:10.1029/2007GL030959.

Fukuda, J. I., and K. M. Johnson (2008), A fully Bayesian inversion for spatial distribution of fault slip with objective smoothing, *Bull. Seismol. Soc. Am.*, *98*(3), 1128–1146, doi:10.1785/0120070194.

Fumal, T. E., M. J. Rymer, and G. G. Seitz (2002), Timing of large earthquakes since A.D. 800 on the Mission Creek strand of the San Andreas Fault Zone at Thousand Palms Oasis, near Palm Springs, California, *Bull. Seismol. Soc. Am.*, *92*(7), 2841–2860, doi:10.1785/0120000609.

Garfunkel, Z. (1974), Model for the late Cenozoic tectonic history of the Mojave Desert, California, and for its relation to adjacent regions, *Geol. Soc. Am. Bull.*, *85*(12), 1931–1944.

Hammond, W. C., C. Kreemer, G. Blewitt, and H.-P. Plag (2010), Effect of viscoelastic postseismic relaxation on estimates of interseismic crustal strain accumulation at Yucca Mountain, Nevada, *Geophys. Res. Lett.*, *37*, L06307, doi:10.1029/2010GL042795.

Hearn, E. H., F. F. Pollitz, W. R. Thatcher, and C. T. Onishi (2013), How do "ghost transients" from past earthquakes affect GPS slip rate estimates on southern California faults?, *Geochem., Geophys., Geosyst.*, *14*(4), 828–838, doi:10.1002/ggge.20080.

Herbert, J. W., M. L. Cooke, M. Oskin, and O. Difo (2013), How much can off-fault deformation contribute to the slip rate discrepancy within the eastern California shear zone?, *Geology*, doi:10.1130/g34738.1.

Herbert, J. W., M. L. Cooke, and S. T. Marshall (2014), Influence of fault connectivity on slip rates in southern California: Potential impact on discrepancies between geodetic derived and geologic slip rates, *J. Geophys. Res. Solid Earth*, *119*, 2342–2361, doi:10.1002/2013JB010472.

Hough, S. E., and K. Hutton (2008), Revisiting the 1872 Owens Valley, California, Earthquake, *Bull. Seismol. Soc. Am.*, *98*(2), 931–949, doi:10.1785/0120070186.

Jackson, D. D., and M. Matsu'ura (1985), A Bayesian approach to nonlinear inversion, *J. Geophys. Res.*, *90*(B1), 581–591, doi:10.1029/JB090iB01p00581.

Jacobs, A., D. Sandwell, Y. Fialko, and L. Sichoix (2002), The 1999 (Mw 7.1) Hector Mine, California, earthquake: Near-field postseismic deformation from ERS interferometry, *Bull. Seismol. Soc. Am.*, *92*(4), 1433–1442, doi:10.1785/0120000908.

Jennings, C. W., and G. J. Saucedo (1994), *Fault Activity Map of California and Adjacent Areas, With Locations and Ages of Recent Volcanic Eruptions*, California Department of Conservation, Division of Mines and Geology, Calif.

Johnson, K. M. (2013), Slip rates and off-fault deformation in Southern California inferred from GPS data and models, *J. Geophys. Res. Solid Earth*, *118*, 5643–5664, doi:10.1002/jgrb.50365.

King, N. E. (1985), Horizontal deformation in the Mojave Desert near Barstow, California, 1979–1983, *J. Geophys. Res.*, *90*(B6), 4491–4494, doi:10.1029/JB090iB06p04491.

Loveless, J. P., and B. J. Meade (2011), Stress modulation on the San Andreas fault by interseismic fault system interactions, *Geology*, doi:10.1130/g32215.1.

Magistrale, H. (2002), Relative contributions of crustal temperature and composition to controlling the depth of earthquakes in Southern California, *Geophys. Res. Lett.*, *29*(10), 1447, doi:10.1029/2001GL014375.

Massonnet, D., W. Thatcher, and H. Vadon (1996), Detection of postseismic fault-zone collapse following the Landers earthquake, *Nature (London)*, *382*(6592), 612–616.

Masterlark, T., and H. F. Wang (2002), Transient stress-coupling between the 1992 Landers and 1999 Hector Mine, California, Earthquakes, *Bull. Seismol. Soc. Am.*, *92*(4), 1470–1486, doi:10.1785/0120000905.

Matmon, A., D. P. Schwartz, R. Finkel, S. Clemmens, and T. Hanks (2005), Dating offset fans along the Mojave section of the San Andreas fault using cosmogenic 26Al and 10Be, *Geol. Soc. Am. Bull.*, *117*(5–6), 795–807, doi:10.1130/b25590.1.

McCaffrey, R. (2005), Block kinematics of the Pacific-North America plate boundary in the southwestern United States from inversion of GPS, seismological, and geologic data, *J. Geophys. Res.*, *110*, B07401, doi:10.1029/2004JB003307.

McClusky, S. C., S. C. Bjornstad, B. H. Hager, R. W. King, B. J. Meade, M. M. Miller, F. C. Monastero, and B. J. Souter (2001), Present day kinematics of the eastern California shear zone from a geodetically constrained block model, *Geophys. Res. Lett.*, *28*(17), 3369–3372, doi:10.1029/2001GL013091.

McGill, S. F., L. A. Owen, R. J. Weldon, and K. J. Kendrick (2013), Latest Pleistocene and Holocene slip rate for the San Bernardino strand of the San Andreas fault, Plunge Creek, Southern California: Implications for strain partitioning within the southern San Andreas fault system for the last ~35 k.y, *Geol. Soc. Am. Bull.*, *125*(1–2), 48–72, doi:10.1130/b30647.1.

Meade, B. J., and B. H. Hager (2005), Block models of crustal motion in Southern California constrained by GPS measurements, *J. Geophys. Res.*, *110*, B03403, doi:10.1029/2004JB003209.

Miller, M. M., D. J. Johnson, T. H. Dixon, and R. K. Dokka (2001), Refined kinematics of the eastern California shear zone from GPS observations, 1993–1998, *J. Geophys. Res.*, *106*(B2), 2245–2263, doi:10.1029/2000JB900328.

Okada, Y. (1985), Surface deformation due to shear and tensile faults in a half-space, *Bull. Seismol. Soc. Am.*, *75*(4), 1135–1154.

Oskin, M., and A. Iriondo (2004), Large-magnitude transient strain accumulation on the Blackwater fault, Eastern California shear zone, *Geology*, *32*(4), 313–316, doi:10.1130/g20223.1.

Oskin, M., L. Perg, E. Shelef, M. Strane, E. Gurney, B. Singer, and X. Zhang (2008), Elevated shear zone loading rate during an earthquake cluster in eastern California, *Geology*, *36*(6), 507–510, doi:10.1130/g24814a.1.

Owen, S., G. Anderson, D. C. Agnew, H. Johnson, K. Hurst, R. Reilinger, Z.-K. Shen, J. Svarc, and T. Baker (2002), Early postseismic deformation from the 16 October 1999 Mw 7.1 Hector Mine, California, earthquake as measured by survey-mode GPS, *Bull. Seismol. Soc. Am.*, *92*(4), 1423–1432, doi:10.1785/0120000930.

Peltzer, G., P. Rosen, F. Rogez, and K. Hudnut (1998), Poroelastic rebound along the Landers 1992 earthquake surface rupture, *J. Geophys. Res.*, *103*(B12), 30,131–30,145, doi:10.1029/98JB02302.

Peltzer, G., F. Crampe, S. Hensley, and P. Rosen (2001), Transient strain accumulation and fault interaction in the Eastern California shear zone, *Geology*, *29*(11), 975–978, doi:10.1130/0091-7613(2001)029<0975:tsaafi>2.0.co;2.

Perfettini, H., and J. P. Avouac (2007), Modeling afterslip and aftershocks following the 1992 Landers earthquake, *J. Geophys. Res.*, *112*, B07409, doi:10.1029/2006JB004399.

Pollitz, F. F. (2003), Transient rheology of the uppermost mantle beneath the Mojave Desert, California, *Earth Planet. Sci. Lett.*, *215*(1–2), 89–104, doi:10.1016/s0012-821x(03)00432-1.

Pollitz, F. F., G. Peltzer, and R. Bürgmann (2000), Mobility of continental mantle: Evidence from postseismic geodetic observations following the 1992 Landers earthquake, *J. Geophys. Res.*, *105*(B4), 8035–8054, doi:10.1029/1999JB900380.

Pollitz, F. F., C. Wicks, and W. Thatcher (2001), Mantle flow beneath a continental strike-slip fault: Postseismic deformation after the 1999 Hector Mine earthquake, *Science*, *293*(5536), 1814–1818, doi:10.1126/science.1061361.

Rolandone, F., R. Bürgmann, and R. M. Nadeau (2004), The evolution of the seismic-aseismic transition during the earthquake cycle: Constraints from the time-dependent depth distribution of aftershocks, *Geophys. Res. Lett.*, *31*, L23610, doi:10.1029/2004GL021379.

Sauber, J., W. Thatcher, and S. C. Solomon (1986), Geodetic measurement of deformation in the central Mojave Desert, California, *J. Geophys. Res.*, *91*(B12), 12,683–12,693, doi:10.1029/JB091iB12p12683.
Sauber, J., W. Thatcher, S. C. Solomon, and M. Lisowski (1994), Geodetic slip rate for the Eastern California shear zone and the recurrence time of Mojave Desert earthquakes, *Nature (London)*, *367*(6460), 264–266.
Savage, J. C. (1983), A dislocation model of strain accumulation and release at a subduction zone, *J. Geophys. Res.*, *88*(B6), 4984–4996, doi:10.1029/JB088iB06p04984.
Savage, J. C., and M. Lisowski (1998), Viscoelastic coupling model of the San Andreas fault along the Big Bend, southern California, *J. Geophys. Res.*, *103*(B4), 7281–7292, doi:10.1029/98JB00148.
Savage, J. C., and R. W. Simpson (2013a), Clustering of velocities in a GPS network spanning the Sierra Nevada Block, the Northern Walker Lane Belt, and the Central Nevada Seismic Belt, California-Nevada, *J. Geophys. Res. Solid Earth*, *118*, 4937–4947, doi:10.1002/jgrb.50340.
Savage, J. C., and R. W. Simpson (2013b), Clustering of GPS velocities in the Mojave block southeastern California, *J. Geophys. Res. Solid Earth*, *118*, 1747–1759, doi:10.1002/jgrb.50053.
Savage, J. C., and J. L. Svarc (1997), Postseismic deformation associated with the 1992 Mw = 7.3 Landers earthquake, southern California, *J. Geophys. Res.*, *102*(B4), 7565–7577, doi:10.1029/97JB00210.
Savage, J. C., and J. L. Svarc (2009), Postseismic relaxation following the 1992 M7.3 Landers and 1999 M7.1 Hector Mine earthquakes, southern California, *J. Geophys. Res.*, *114*, B01401, doi:10.1029/2008JB005938.
Savage, J. C., M. Lisowski, and W. H. Prescott (1990), An apparent shear zone trending north-northwest across the Mojave Desert into Owens Valley, eastern California, *Geophys. Res. Lett.*, *17*(12), 2113–2116, doi:10.1029/GL017i012p02113.
Savage, J. C., M. Lisowski, and M. Murray (1993), Deformation from 1973 through 1991 in the epicentral area of the 1992 Landers, California, Earthquake (Ms = 7.5), *J. Geophys. Res.*, *98*(B11), 19,951–19,958, doi:10.1029/93JB02029.
Savage, J. C., W. Gan, and J. L. Svarc (2001), Strain accumulation and rotation in the Eastern California Shear Zone, *J. Geophys. Res.*, *106*(B10), 21,995–22,007, doi:10.1029/2000JB000127.
Savage, J. C., J. L. Svarc, and W. H. Prescott (2003), Near-field postseismic deformation associated with the 1992 Landers and 1999 Hector Mine, California, earthquakes, *J. Geophys. Res.*, *108*(B9), 2432, doi:10.1029/2002JB002330.
Scientists from the U.S. Geological Survey, Southern California Earthquake Center, and C. D. o. M. Geology (2000), Preliminary report on the 16 October 1999 M 7.1 Hector Mine, California, earthquake, *Seismol. Res. Lett.*, *71*(1), 11–23, doi:10.1785/gssrl.71.1.11.
Segall, P., and M. V. Matthews (1988), Displacement calculations from geodetic data and the testing of geophysical deformation models, *J. Geophys. Res.*, *93*(B12), 14,954–14,966, doi:10.1029/JB093iB12p14954.
Shen, Z. K., R. W. King, D. C. Agnew, M. Wang, T. A. Herring, D. Dong, and P. Fang (2011), A unified analysis of crustal motion in Southern California, 1970–2004: The SCEC Crustal Motion Map, *J. Geophys. Res.*, *116*, B11402, doi:10.1029/2011JB008549.
Shen, Z., D. Agnew, R. King, D. Dong, T. Herring, M. Wang, H. Johnson, G. Anderson, R. Nikolaidis, and M. van Domselaar (2003), The SCEC crustal motion map, version 3.0, edited.
Shen, Z.-K., D. D. Jackson, Y. Feng, M. Cline, M. Kim, P. Fang, and Y. Bock (1994), Postseismic deformation following the Landers earthquake, California, 28 June 1992, *Bull. Seismol. Soc. Am.*, *84*(3), 780–791.
Shen, Z.-K., D. D. Jackson, and B. X. Ge (1996), Crustal deformation across and beyond the Los Angeles basin from geodetic measurements, *J. Geophys. Res.*, *101*(B12), 27,957–27,980, doi:10.1029/96JB02544.
Shen, Z.-K., D. Dong, T. A. Herring, K. Hudnut, D. Jackson, R. King, S. C. McClusky, and L.-Y. Sung (1997), Crustal deformation measured in Southern California, *Eos Trans. Am. Geophys. Union*, *78*(43), 477–482.
Shen, Z.-K., D. D. Jackson, and Y. Y. Kagan (2007), Implications of geodetic strain rate for future earthquakes, with a five-year forecast of M5 earthquakes in Southern California, *Seismol. Res. Lett.*, *78*(1), 116–120, doi:10.1785/gssrl.78.1.116.
Sieh, K., et al. (1993), Near-Field Investigations of the Landers earthquake sequence, April to July 1992, *Science*, *260*(5105), 171–176, doi:10.1126/science.260.5105.171.
Simpson, R. W., W. Thatcher, and J. C. Savage (2012), Using cluster analysis to organize and explore regional GPS velocities, *Geophys. Res. Lett.*, *39*, L18307, doi:10.1029/2012GL052755.
Snay, R. A., M. W. Cline, C. R. Philipp, D. D. Jackson, Y. Feng, Z.-K. Shen, and M. Lisowski (1996), Crustal velocity field near the big bend of California's San Andreas fault, *J. Geophys. Res.*, *101*(B2), 3173–3185, doi:10.1029/95JB02394.
Spinler, J. C., R. A. Bennett, M. L. Anderson, S. F. McGill, S. Hreinsdóttir, and A. McCallister (2010), Present-day strain accumulation and slip rates associated with southern San Andreas and eastern California shear zone faults, *J. Geophys. Res.*, *115*, B11407, doi:10.1029/2010JB007424.
Stein, R. S., and M. Lisowski (1983), The 1979 Homestead Valley earthquake sequence, California: Control of aftershocks and postseismic deformation, *J. Geophys. Res.*, *88*(B8), 6477–6490, doi:10.1029/JB088iB08p06477.
Toppozada, T. R., D. M. Branum, M. S. Reichle, and C. L. Hallstrom (2002), San Andreas Fault Zone, California: M ≥5.5 earthquake history, *Bull. Seismol. Soc. Am.*, *92*(7), 2555–2601, doi:10.1785/0120000614.
van der Woerd, J., Y. Klinger, K. Sieh, P. Tapponnier, F. J. Ryerson, and A.-S. Mériaux (2006), Long-term slip rate of the southern San Andreas fault from 10Be-26Al surface exposure dating of an offset alluvial fan, *J. Geophys. Res.*, *111*, B04407, doi:10.1029/2004JB003559.
Weldon, R. J., T. E. Fumal, T. J. Powers, S. K. Pezzopane, K. M. Scharer, and J. C. Hamilton (2002), Structure and earthquake offsets on the San Andreas fault at the Wrightwood, California, paleoseismic site, *Bull. Seismol. Soc. Am.*, *92*(7), 2704–2725, doi:10.1785/0120000612.
Wessel, P., and W. Smith (1998), New, improved version of Generic Mapping Tools released, *Eos Trans. AGU*, *79*, 579.
Yule, D., and K. Sieh (2003), Complexities of the San Andreas fault near San Gorgonio Pass: Implications for large earthquakes, *J. Geophys. Res.*, *108*(B11), 2548, doi:10.1029/2001JB000451.
Zeng, Y., and Z.-K. Shen (2014), Fault network modeling of crustal deformation in California constrained using GPS and geologic observations, *Tectonophysics*, *612*, 1–17.